Draft version July 6, 2021
Typeset using LaTeX **twocolumn** style in AASTeX63

New constraints on the interstellar medium and the associated outflow in the z=6.42 quasar J1148+5251

Romain A. Meyer,[1] Fabian Walter,[1] Pierre Cox,[2] Roberto Decarli,[3] Roberto Neri,[4] Mladen Novak,[1] Antonio Pensabene,[3] Dominik Riechers,[5] and Axel Wei[6]

[1] *Max Planck Institute for Astronomy, Knigstuhl 17, D-69117, Heidelberg, Germany*
[2] *Sorbonne Universit, UPMC Universit Paris 6 and CNRS, UMR 7095, Institut dAstrophysique de Paris, 98bis Boulevard Arago,75014 Paris, France*
[3] *INAF Osservatorio di Astrofisica e Scienza dello Spazio di Bologna, via Gobetti 93/3, I-40129, Bologna, Italy*
[4] *Institut de Radioastronomie Millimtrique (IRAM), 300 Rue de la Piscine, 38400 Saint-Martin-dHéres, France*
[5] *Cornell University, Space Sciences Building, Ithaca, NY 14853, USA*
[6] *Max-Planck-Institut für Radioastronomie, Auf dem Hügel 71, 53121 Bonn, Germany*

(Received XX; Revised July 6, 2021; Accepted XX)

Submitted to AJ

ABSTRACT

We report new Northern Extended Millimeter Array (NOEMA) observations of the [C II]$_{158\,\mu\mathrm{m}}$, [N II]$_{205\,\mu\mathrm{m}}$ and [O I]$_{146\,\mu\mathrm{m}}$ atomic fine structure lines and dust continuum emission of J1148+5251, a $z = 6.42$ quasar, that probe the physical properties of its interstellar medium (ISM). The [C II]$_{158\,\mu\mathrm{m}}$ and dust continuum emission have similar extensions up to ~ 2.5" (or ~ 9 kpc, accounting for beam–convolution) suggesting that they both trace the extent of the host galaxy. However, the new data neither recover the broad [C II]$_{158\,\mu\mathrm{m}}$ line–widths nor the [C II]$_{158\,\mu\mathrm{m}}$ emission on significantly larger spatial scales (up to ~ 30 kpc) described in earlier studies. We also report the first detection of the [O I]$_{146\,\mu\mathrm{m}}$ and (tentatively) [N II]$_{205\,\mu\mathrm{m}}$ emission lines in J1148+5251. Using Fine Structure Lines (FSL) ratios of the [C II]$_{158\,\mu\mathrm{m}}$, [N II]$_{205\,\mu\mathrm{m}}$, [O I]$_{146\,\mu\mathrm{m}}$ and [C I]$_{370\mu\mathrm{m}}$ emission lines, we show that J1148+5251 has similar ISM conditions compared to lower–redshift (ultra)-luminous infrared galaxies. CLOUDY modelling of the FSL ratios exclude X–ray dominated regions (XDR) and favours photodissociation regions (PDR) as the origin of the FSL emission. We find that a high radiation field ($10^{3.5-4.5}\,G_0$), high gas density ($n \simeq 10^{3.5-4.5}\,\mathrm{cm}^{-3}$) and HI column density of $10^{23}\,\mathrm{cm}^{-2}$ reproduce the observed FSL ratios well. J1148+5251 is ultimately a standard $z > 6$ luminous quasar only distinguished by its extended [C II]$_{158\,\mu\mathrm{m}}$ and dust emission, twice larger than that of any other quasar at these early times.

Keywords: galaxies: high–redshift — galaxies: ISM — quasars: emission lines — galaxies: individual (SDSS J1148+5251)

1. INTRODUCTION

Luminous quasar activity is a key process of galaxy evolution. Indeed, massive outflows driven by the radiation pressure generated by the accretion of gas onto the central supermassive black hole (SMBH), or so–called Active Galactic Nuclei (AGN) feedback", are invoked in most models of galaxy formation to clear massive galaxies of their gas and quench star formation (e.g., Silk & Rees 1998; Di Matteo et al. 2005; Springel et al. 2005; King 2010; Costa et al. 2014; Ishibashi & Fabian 2015; Richardson et al. 2016; Negri & Volonteri 2017; Oppenheimer et al. 2020; Koudmani et al. 2021). Luminous quasars are most interesting at high–redshift in particular, when they probe the early phase of co–evolution between the first galaxies and their central black hole. The advent of large optical and infrared surveys has enabled the discovery of quasars up to $z \sim 7.5$ (Bañados

Corresponding author: Romain A. Meyer
meyer@mpia.de

et al. 2018; Yang et al. 2020; Wang et al. 2021), with several hundreds at $z > 6$ (see Bosman 2020, for an up–to–date list). These early quasars harbour SMBHs with $M_\bullet \gtrsim 10^8\,\mathrm{M}_\odot$ and accrete gas at or near the Eddington limit for most of their life, challenging models of SMBH formation and growth (e.g., De Rosa et al. 2014; Bañados et al. 2018; Mazzucchelli et al. 2017; Wang et al. 2021). Because the bright quasar light outshines that of the host in the optical and near–infrared, the galaxies hosting early luminous quasars have remained relatively mysterious until the advent of modern (sub–)millimeter observatories.

Numerous observations of $z > 6$ quasars targeting the bright Far–Infrared (FIR) [C II]$_{158\,\mu\mathrm{m}}$ emission line have revealed their host galaxies tobe infrared luminous, dusty and actively forming stars with estimated rates of $10^2 - 10^3 M_\odot \mathrm{yr}^{-1}$ (e.g., Walter et al. 2003, 2009a; Maiolino et al. 2005, 2012; Bañados et al. 2015; Decarli et al. 2018; Venemans et al. 2018, 2020; Novak et al. 2019, 2020; Wang et al. 2013, 2019; Yang et al. 2020). [C II]$_{158\,\mu\mathrm{m}}$ kinematics also show that most quasar hosts are massive galaxies ($M_* \sim 10^{10}\,M_\odot$) displaying a variety of morphologies such as stable disks, bulge–dominated galaxies and mergers with nearby companions (Shao et al. 2017, 2019; Wang et al. 2013, 2019; Decarli et al. 2019a,b; Neeleman et al. 2019, 2021). The report of broad [C II]$_{158\,\mu\mathrm{m}}$line wings in the z=6.42 quasar J1148+5251 (Maiolino et al. 2012; Cicone et al. 2015) spurred the use of the [C II]$_{158\,\mu\mathrm{m}}$ emission line to identify quasar outflow signatures in the early Universe. Such features have however remained rare, and stacking analyses have led to contradictory results (Bischetti et al. 2019; Novak et al. 2020). Recently, Izumi et al. (2021a,b) reported broad [C II]$_{158\,\mu\mathrm{m}}$ line wings in two low-luminosity quasars at $z = 6.72$ and $z = 7.07$.

Two decades of [C II]$_{158\,\mu\mathrm{m}}$ and CO studies have shown that early luminous quasars provide an unparalleled observational window into the physics of the earliest (and most massive) galaxies in the Universe. However, multi–line studies using lines other than [C II]$_{158\,\mu\mathrm{m}}$ and CO transitions have been much rarer until now. Since different fine structure lines (FSL) trace different gas densities and excitation levels, only in combination can they probe the ionized and neutral atomic gas phases, and the excitation source(s) of the gas (e.g., Carilli & Walter 2013, for a review). Besides [C II]$_{158\,\mu\mathrm{m}}$, potential atomic fine structure lines of interest include [N II]$_{122\,\mu\mathrm{m}}$, [N II]$_{205\,\mu\mathrm{m}}$, [O I]$_{63\,\mu\mathrm{m}}$, [O I]$_{145\,\mu\mathrm{m}}$ [O III]$_{88\,\mu\mathrm{m}}$ and [C I]$_{369\,\mu\mathrm{m}}$, all accessible at $z \sim 6$ with (sub–)millimeter arrays such as the Atacama Large Millimeter Array (ALMA) or the Northern Extended Millimeter Array (NOEMA). Moreover, these lines have been observed with *Herschel* in large samples of local (ultra)-luminous infrared galaxies -(U)LIRGs, which can which can be readily compared to $z \sim 6$ quasars (e.g., Díaz-Santos et al. 2017; Herrera-Camus et al. 2018).

Detections of FSL other than [C II]$_{158\,\mu\mathrm{m}}$ in $z > 6$ quasars are still relatively recent (Walter et al. 2018; Hashimoto et al. 2019; Novak et al. 2019; Li et al. 2020), and a complex picture is emerging from these first results. Emission lines probing the neutral phase ([O I]$_{145\,\mu\mathrm{m}}$ and [C I]$_{369\,\mu\mathrm{m}}$) show good agreement between the line ratios and line–to–far–infrared (FIR) ratios of distant quasars and local (U)LIRGs (Novak et al. 2019; Li et al. 2020). However in two $z > 6$ quasars the ratio of [O III]$_{88\,\mu\mathrm{m}}$ to [C II]$_{158\,\mu\mathrm{m}}$, probing the ionized gas phase, presents a mild excess (factor 2–3) with respect to local (U)LIRGS (Novak et al. 2019; Li et al. 2020) and high–redshift galaxies (Hashimoto et al. 2019). This is however not true for the quasar J2100–1715 and its companion galaxy (e.g., Walter et al. 2018). Clearly, more FIR multi–line studies of $z > 6$ quasars are needed to understand the ISM of their host galaxies.

SDSS J1148+5251 is one of the earliest high–redshift quasars discovered in the SDSS survey (Fan et al. 2003, z=6.4189), and harbours a $3 \times 10^9 M_\odot$ SMBH (Willott et al. 2003). Being the redshift record–holder for many years after its discovery, it was extensively observed with the Very Large Array and the IRAM Plateau de Bure Interferometer (PdBI) and was the first object detected in CO and [C II]$_{158\,\mu\mathrm{m}}$ at $z > 5$ (Walter et al. 2003, 2004; Bertoldi et al. 2003b,a; Maiolino et al. 2005; Riechers et al. 2009; Walter et al. 2009a,b). These pioneering studies probed the host galaxy Star Formation Rate (SFR), dust and ISM properties. Additionally, Maiolino et al. (2012) and Cicone et al. (2015) reported the presence of a broad [C II]$_{158\,\mu\mathrm{m}}$ emission ($\sigma_v = 900\,\mathrm{km\,s}^{-1}$) component in the PdBI data, suggesting the presence of an outflow as well as spatially extended [C II]$_{158\,\mu\mathrm{m}}$ emission (up to $r \sim 30$ kpc). In this paper, we return to J1148+5251 with a new set of NOEMA observations, capitalizing on larger bandwidths and more antennas, thus improving on the image fidelity as compared to earlier PdBI observations. The new observations targeted atomic fine structure emission lines ([O I]$_{146\,\mu\mathrm{m}}$, [N II]$_{205\,\mu\mathrm{m}}$) and other molecular (CO, H_2O) rotational transitions. The aim of the observations was to dissect the ISM phases without relying on assumptions about the origin of [C II]$_{158\,\mu\mathrm{m}}$ which can come from both the ionized and neutral phases. Indeed, [O I]$_{146\,\mu\mathrm{m}}$ traces exclusively the neutral phase/ photo–dissociated regions (PDRs), whereas [N II]$_{205\,\mu\mathrm{m}}$ traces the ionized/H II regions. This set of observations is complemented with earlier $[\mathrm{C\ I}]_{370\mu\mathrm{m}}$ data (Riechers et al. 2009) that trace the neutral/molecular gas. Thanks to the wave spectral coverage of the new NOEMA correlator *PolyFix* and the upgraded NOEMA array, these observations achieved a high–fidelity that resulted in deep $[\mathrm{C\ II}]_{158\,\mu\mathrm{m}}$ observations and tight constraints on the underlying dust continuum.

The structure of this paper is as follows. We present in Section 2 and 3 the new observations of the $[\mathrm{C\ II}]_{158\,\mu\mathrm{m}}$, $[\mathrm{N\ II}]_{205\,\mu\mathrm{m}}$ and $[\mathrm{O\ I}]_{146\,\mu\mathrm{m}}$ emission lines in J1148+5251 as well as the FIR continuum observed between 200 and 280 GHz. We focus on the $[\mathrm{C\ II}]_{158\,\mu\mathrm{m}}$ emission line to investigate its reported broad velocity component and spatial extension in Section 4. In Section 5, we derive ISM properties from the strength of the atomic fine-structure emission lines observed, before concluding our study in Section 6. Throughout this paper, we assume a concordance cosmology with $H_0 = 70\,\mathrm{km\,s^{-1}Mpc^{-1}}$, $\Omega_M = 0.3, \Omega_\Lambda = 0.7$. At the redshift of the target ($z = 6.42$), 1" corresponds to 5.62 proper kpc.

2. OBSERVATIONS AND DATA REDUCTION

We have observed the z=6.4189 quasar J1148+5251 using NOEMA (Project ID: w17ex001/w17ex001, PI: F. Walter). The pointing and phase center of our observations were chosen to correspond to the quasar position in the optical SDSS imaging (RA = 11:48:16.64, DEC = +52:51:50.32). The observations included two spectral setups taking advantage of the new *PolyFix* correlator covering simultaneously two 7.744 GHz–wide sidebands [1]. The first spectral setup was centered at 267 GHz such that the lower sideband (255 − 263 GHz) covers the redshifted $[\mathrm{C\ II}]_{158\,\mu\mathrm{m}}$ emission with one sideband whilst the upper sideband (271 − 279 GHz) covers the $[\mathrm{O\ I}]_{146\,\mu\mathrm{m}}$ emission. The second setup was centered at 208 GHz to cover the $[\mathrm{N\ II}]_{205\,\mu\mathrm{m}}$ in the lower sideband (196 − 204 GHz). The setups also covered two high–J CO (14-13 and 13-12) and H_2O rotational transitions ($5_{23} - 4_{32}$ and $3_{22} - 3_{13}$), which will be discussed in future works. The observations were executed between December 2017 and May 2018. The $[\mathrm{C\ II}]_{158\,\mu\mathrm{m}}$ and $[\mathrm{O\ I}]_{146\,\mu\mathrm{m}}$ setup was mostly observed in configuration 9D except for two tracks using 8 antennas (with baselines ranging from 24m to 176m), for a total observing time of 18.7h. Data was (remotely) reduced at IRAM Grenoble using the *CLIC* package within the GILDAS framework (jan2021a version)[2]. We reach a rms noise of 0.64(0.88) mJy beam^{-1} in $50\,\mathrm{km\,s^{-1}}$ channels, and the synthesized beam size is 1.89" × 1.59" (1.83" × 1.51") for the $[\mathrm{C\ II}]_{158\,\mu\mathrm{m}}$($[\mathrm{O\ I}]_{146\,\mu\mathrm{m}}$) line observations. The $[\mathrm{N\ II}]_{205\,\mu\mathrm{m}}$ and CO lines were observed with 8 antennas for a total of 15.7h with baselines ranging from 24m to 176m. For the $[\mathrm{N\ II}]_{205\,\mu\mathrm{m}}$ line the noise rms is 0.78 mJy beam^{-1} in $50\,\mathrm{km\,s^{-1}}$ channels and the synthesized beam size 1.79" × 1.51". For the continuum, the synthesized beam size achieved is 1.78" × 1.51", 1.65" × 1.46", 1.91" × 1.71" and 1.88" × 1.52" at 200, 212, 259 and 272 GHz.

Imaging and cleaning was performed using the latest version of MAPPING/GILDAS (jan2021a). The dirty maps were obtained from the visibilities without tapering and using natural weighting. Cleaning was performed down to 2σ (where σ is the rms noise in the dirty map) using a circular clean region of radius $r = 5$". The reason for choosing such a wide radius are the earlier reports of extended $[\mathrm{C\ II}]_{158\,\mu\mathrm{m}}$ emission (Maiolino et al. 2012; Cicone et al. 2015). An additional clean region with radius $r = 2$" was added on the NW source reported by Leipski et al. (2010) and Cicone et al. (2015) which is also detected in our data [3]. The final products were created using the following procedure. Firstly, data cubes with $50\,\mathrm{km\,s^{-1}}$ channels were produced to find significant emission lines. The $[\mathrm{C\ II}]_{158\,\mu\mathrm{m}}$, $[\mathrm{N\ II}]_{205\,\mu\mathrm{m}}$, $[\mathrm{O\ I}]_{146\,\mu\mathrm{m}}$, H_2O ($5_{23} - 4_{32}$ and $3_{22} - 3_{13}$,ν_{rest} =258.7 GHz), CO(14-13) and CO(13-12) emission lines were fitted with a single Gaussian profile in order to estimate their FWHM. Continuum maps were created using all channels at least 1.25×FWHM away from each emission line. The continuum, determined from the line–free channels using an order 1 interpolation (GILDAS *UV_BASELINE* routine) over the ∼ 7.6 GHz sidebands, was subtracted in the *uv* plane to create continuum–subtracted cubes.

In order to determine the significance of emission lines, velocity–integrated emission line maps (line maps") were created by integrating channels over 1.2 times the FWHM of the $[\mathrm{C\ II}]_{158\,\mu\mathrm{m}}$ line (i.e., $482\,\mathrm{km\,s^{-1}}$) at the redshifted frequency of the line. We use the $[\mathrm{C\ II}]_{158\,\mu\mathrm{m}}$ redshift ($z = 6.4189$) to determine redshifted frequency of all lines. Such maps, assuming the line is Gaussian,

[1] https://www.iram-institute.org/EN/content-page-96-7-56-96-0-0.html

[2] https://www.iram.fr/~gildas/dist/

[3] We found no emission lines for this source in any of the spectral setups used in this work.

contain by definition 84% of the total flux[4] (see for a short derivation appendix A of Novak et al. (2020)) . All total line fluxes measured from the line maps and reported in this paper are accounting for this effect. Additionally, all continuum and line fluxes in this paper were computed using the residual scaling method (e.g., Jorsater & van Moorsel 1995; Walter & Brinks 1999; Walter et al. 2008; Novak et al. 2019).

In order to determine the aperture needed to recover most of the flux of the emission lines and the dust continuum, a curve of growth approach was adopted. We show in Appendix A that all line and continuum fluxes reach a maximum or plateau at an aperture radius $r = 3$", which corresponds to 16.9 kpc at $z = 6.42$. A nominal aperture radius of 3" is thus adopted throughout the paper. The line subtraction procedure described above was repeated using the $r = 3$" aperture to obtain final produces. Additionally, we have investigated the use of Multiscale cleaning in appendix B. We conclude that the [C II]$_{158\,\mu\mathrm{m}}$ emission and the $259 - 272$ GHz continuum are better recovered using Multiscale cleaning, and we therefore use Multiscale cleaning with Gildas/MAPPING for these data throughout the paper.

3. RESULTS

3.1. *Dust continuum emission*

We first present the FIR continuum maps in Figure 1. The FIR continuum is clearly detected in all four sidebands. The measured continuum flux densities are tabulated in Table 1. Due to the upgraded bandwidth of the NOEMA *PolyFix* correlator, these continuum measurements have higher sensitivity than previous observations at ~ 260 GHz (Walter et al. 2009a; Maiolino et al. 2012; Cicone et al. 2015). The new continuum flux density at 259 GHz ($4.64 \pm 0.26\,\mathrm{mJy}$) is in good agreement[5] with the earlier PdBI measurement from Walter et al. (2009a) and the 1.2 mm continuum measurement ($5.0 \pm 0.6\,\mathrm{mJy}$, Bertoldi et al. 2003a). We combine our new continuum measurements with previous literature results (Bertoldi et al. 2003b; Walter et al. 2003; Robson et al. 2004; Riechers et al. 2009; Leipski et al. 2010; Maiolino et al. 2012; Gallerani et al. 2014; Cicone et al. 2015) to fit the FIR spectral energy distribution.

ν_{obs} [GHz]	S_ν [mJy]	rms [mJy]	Beam size
200	1.78 ± 0.23	0.06	1.78" × 1.51"
216	2.33 ± 0.21	0.05	1.65" × 1.46"
259	4.64 ± 0.26	0.08	1.91" × 1.71"
274	5.85 ± 0.29	0.08	1.88" × 1.52"

Table 1. Continuum measurements at $200 - 274$ GHz extracted from the continuum images (Figure 1, effective bandwidth $\simeq 7.68$ GHz (masking the edges and central baseband gap) and integrated in a circular aperture with radius $r = 3$".

Assuming optically thin dust emission at $\lambda > 40\mu$m (e.g., Beelen et al. 2006), we use a modified black body model for the dust emission and correct both for contrast and CMB heating as prescribed by Da Cunha et al. (2013). The dust mass is derived assuming an opacity $\kappa_{\nu_{rest}} = \kappa_{\nu_0}(\nu_{rest}/\nu_0)^\beta$ with $\nu_0 = c/(125\mu\mathrm{m})$ and $\kappa_0 = 2.64\mathrm{m}^2\mathrm{kg}^{-1}$ following Dunne et al. (2003) with β being the dust spectral emissivity index. Our purpose is primarily to measure the cold dust FIR luminosity to constrain the SFR in J1148+5251. Therefore, we omit data points at $\nu_{\mathrm{rest}} > 1000\,\mathrm{GHz}(\lambda_{\mathrm{rest}} \lesssim 125\,\mu\mathrm{m})$ which are potentially contaminated by the quasar non–thermal and warm dust emission (e.g., Leipski et al. 2010). The dust SED model uses three free parameters (total dust mass M_d, dust emissivity index β, dust temperature T_d) and is fitted using MCMC with the *emcee* package (Foreman-Mackey et al. 2013) The resulting best–fit and observational constraints are shown in Figure 2 and the posterior probability distribution of the dust SED parameters is displayed in Appendix C. The median dust mass is $3.2 \times 10^8 M_\odot$ and the median dust temperature is moderately high ($T_d = 51.3$ K), in agreement with earlier studies (e.g., Beelen et al. 2006; Leipski et al. 2010; Cicone et al. 2015), which is not surprising considering that most of the constraining power comes from observations at lower and higher frequencies than those reported in this work.

We integrate the modified black body to derive the total infrared (IR, $8 - 1000\,\mu$m) and far–infrared (FIR, $42.5 - 122.5\mu$m, e.g., Helou et al. 1985) luminosities. The total infrared luminosity is $L_{\mathrm{IR}} = (20.9 \pm 6.8) \times 10^{12} L_\odot$ and the far–infrared luminosity $L_{\mathrm{FIR}} = (13.4 \pm 2.4) \times 10^{12} L_\odot$, in agreement with earlier studies of J1148+5251. Indeed, assuming that dust heating is dominated by young stars, the infrared luminosity can be converted to a SFR using the Kennicutt (1998) and Kennicutt & Evans (2012) conversions, giving SFR= $(1830 \pm 595) - (2090 \pm 680) M_\odot\,\mathrm{yr}^{-1}$, respectively. This is in agreement with earlier studies which found that

[4] We have checked that this correction holds for the [C II]$_{158\mu\mathrm{m}}$ emission where the flux recovered in a $(-1500, +1500)\,\mathrm{km\,s^{-1}}$ velocity-integrated map is $S_{\mathrm{line}}\Delta v = 10.5 \pm 0.92\,\mathrm{mJy\,km\,s^{-1}}$ and the 1/0.84–corrected flux in the nominal 1.2×FWHM$_{\mathrm{[C\ II]}}$ = $482\,\mathrm{km\,s^{-1}}$ channel is $S_{\mathrm{line}}\Delta v = 10.4 \pm 0.5\,\mathrm{mJy\,km\,s^{-1}}$, where S_{line} is integrated in a circular aperture with $r = 3$". Indeed, the choice of a 1.2×FWHM–wide channel maximises the SNR without flux losses.

[5] We have checked that there is no continuum offset between the two side–bands by imaging the calibrators (1150+497 and 1216+487) for every track and the stacked data.

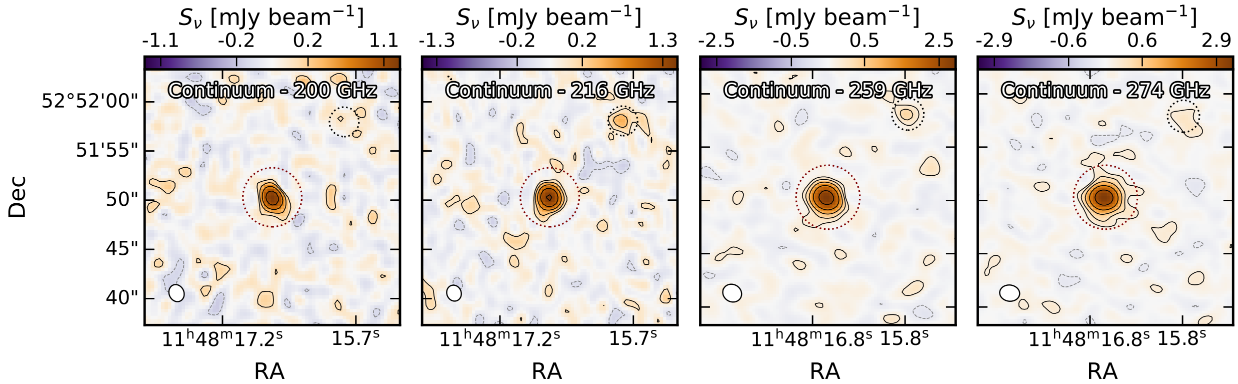

Figure 1. Dust continuum emission maps integrated over the ~ 7.68 GHz of the *PolyFix* correlator effective bandwidth for each sideband with central frequency $200, 216, 259$ and 274 GHz. The dotted circle centred on J1148+5251 indicates the aperture raidus of 3" adopted throughout this paper for flux density estimates. An additional source, reported previously by Leipski et al. (2010) and Cicone et al. (2015) is visible in the three higher–frequency bands at $\sim$ 10" to the north–west (black dotted circle). The contours are logarithmic $(-4, -2, 2, 4, 8, 16, 32)\sigma$ (rms). The colour scaling is log–linear, the threshold being at 3σ.

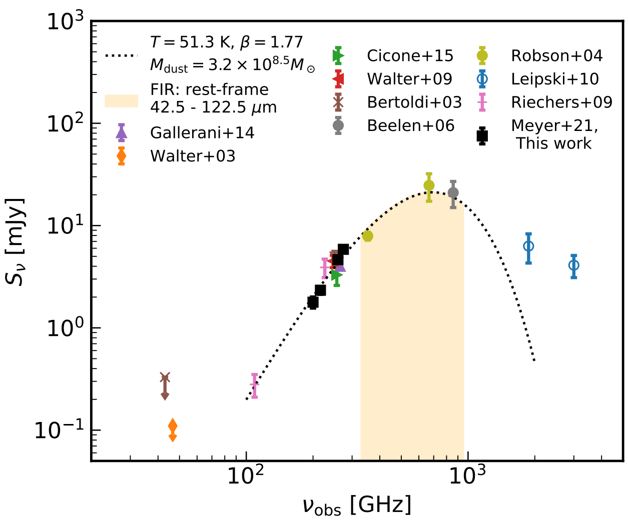

Figure 2. Continuum measurements from the literature and this work with the best–fit modified black body dust emission model. The effect of the CMB is accounted for as prescribed by Da Cunha et al. (2013) and the data points at $\nu > 10^3$ GHz are not used for the fit. The FIR luminosity, integrated over the shaded orange area, is not significantly affected by this choice.

J1148+5251 is in an intense starburst phase (Maiolino et al. 2005; Walter et al. 2009a; Maiolino et al. 2012; Cicone et al. 2015).

3.2. *Fine structure line detections*

We present the line maps for the [C II]$_{158\,\mu m}$, [O I]$_{146\,\mu m}$ and [N II]$_{205\,\mu m}$ emission in Figure 3. For comparison, we also show maps of the same channel width ($482\,\mathrm{km\,s^{-1}}$) than the main line map but offset by $\pm 482\,\mathrm{km\,s^{-1}}$ from the line emission to visually assess the robustness of our detections. The spectra of the [C II]$_{158\,\mu m}$ line are presented in Figures 5 (see also Appendix D), whilst the [O I]$_{146\,\mu m}$ and [N II]$_{205\,\mu m}$ spectra are shown in Fig. 4. The FWHM of the detected [O I]$_{146\,\mu m}$ and [N II]$_{205\,\mu m}$ lines are consistent with that of the [C II]$_{158\,\mu m}$ line (i.e., $\sim 400\mathrm{km\,s^{-1}}$).

We detect [C II]$_{158\,\mu m}$ and [O I]$_{146\,\mu m}$ at 42σ and 5.3σ (where the SNR is calculated using the peak surface brightness in the line maps and the pixel rms level). [N II]$_{205\,\mu m}$ is only marginally detected (3.7σ) in the $r =$ 3" aperture and its peak emission could be offset from the rest–frame UV, dust, [C II]$_{158\,\mu m}$, and [O I]$_{146\,\mu m}$ emission. In the central pixel of the [C II]$_{158\,\mu m}$ emission, [N II]$_{205\,\mu m}$ is formally undetected. We defer further discussion of the [N II]$_{205\,\mu m}$ emission line to section 5.2. In our subsequent analysis of the ISM of J1148+5251, we focus on the extended aperture–integrated fluxes. All the fluxes and derived line luminosities are tabulated in Table. 2. For comparison, we have also measured the flux density of the [C II]$_{158\,\mu m}$ emission by fitting the aperture–integrated spectrum with a Gaussian, and show a comparison between our work and earlier studies for various aperture sizes in Appendix D. In summary, we find a good agreement between the line map flux estimates and the spectrum best-fits values, as well as good agreement between previous studies and the data presented here, as long as the core" (< 3" emission, no velocity offsets) [C II]$_{158\,\mu m}$ emission is considered.

4. THE SPATIAL AND VELOCITY STRUCTURE OF THE [C II]$_{158\,\mu m}$ EMISSION IN J1148+5251

4.1. *Spectral analysis*

Figure 5 shows the continuum–subtracted [C II]$_{158\,\mu m}$ spectrum (extracted in a $r = 3$" aperture), as well as single and double Gaussian fits to the data. We found an emission feature at 262.2 GHz rest-frame which subse-

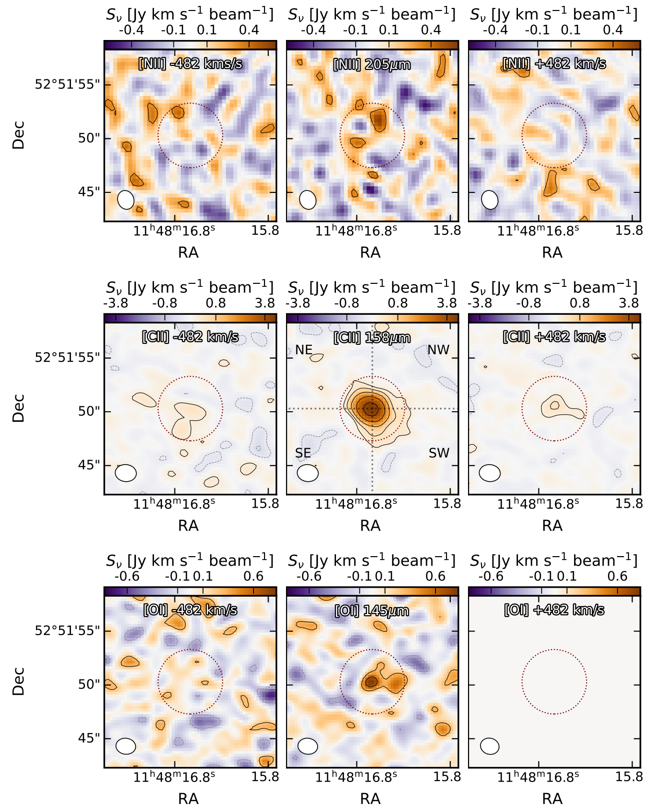

Figure 3. Line maps, velocity–integrated over $1.2\times$ FWHM$_{[\mathrm{C\ II}]}$ $=482\,\mathrm{km\,s^{-1}}$ at the expected frequency of [C II]$_{158\,\mu\mathrm{m}}$, [N II]$_{205\,\mu\mathrm{m}}$ and [O I]$_{146\,\mu\mathrm{m}}$ and assuming the [CII] redshift. For each line, we also plot two additional collapsed maps centered at $\pm482\,\mathrm{km\,s^{-1}}$ away from the line emission. For [O I]$_{146\,\mu\mathrm{m}}$ only one of the adjacent maps is empty as the emission is at the edge of the band. On the central [C II]$_{158\,\mu\mathrm{m}}$ map we plot the quadrants used for the spatial extension analysis in Section 4.2. The contours are logarithmic $(-4,-2,2,4,8,16,32)\sigma$ (rms).

quently was masked to determine and subtract the continuum. An emission line map of the feature does not reveal any convincing line. We checked that masking this feature or not does not impact our results. We find that a single Gaussian describes the [C II]$_{158\,\mu\mathrm{m}}$ emission well, and that the single Gaussian residuals are consistent with the rms noise. The best–fit double Gaussian model [6] differs very little from the simpler model, and the residuals are nearly identical (Fig. 5, lower right). The χ^2 improvement obtained with a double Gaussian is $\Delta\chi^2 = 2.24$, which for an increase of 3 free parameters gives a p–value of 0.46 of rejecting the simple model in favor of a double Gaussian. We thus do not find evidence

[6] In the best-fit double Gaussian model, the broad component has the following parameters: $\Delta v = 80\pm350\,\mathrm{km\,s^{-1}}$, $S_{\mathrm{peak}} = 1.5\pm4.0\,\mathrm{Jy\,km\,s^{-1}}$,FWHM$_{\mathrm{broad}} = 960\pm1100\,\mathrm{km\,s^{-1}}$.

3” aperture	[N II]$_{205\,\mu\mathrm{m}}$	[C II]$_{158\,\mu\mathrm{m}}$	[O I]$_{146\,\mu\mathrm{m}}$
S/N	3.7	42.0	5.4
$S_{line}\Delta v$ [Jy km s^{-1}]	0.5 ± 0.3	10.2 ± 0.5	1.0 ± 0.6
L_{line} [$10^9 L_\odot$]	0.4 ± 0.2	10.6 ± 0.5	1.1 ± 0.7
L'_{line}[10^9 K km s^{-1}pc^{-2}]	4.4 ± 2.1	48.1 ± 2.5	4.1 ± 2.4
Peak [CII] pixel	**[N II]$_{205\,\mu\mathrm{m}}$**	**[C II]$_{158\,\mu\mathrm{m}}$**	**[O I]$_{146\,\mu\mathrm{m}}$**
S/N	1.1	42.0	5.4
$S_{line}\Delta v$ [Jy km s^{-1}]	<0.12	6.4 ± 0.2	1.0 ± 0.2
L_{line} [$10^9 L_\odot$]	<0.10	6.7 ± 0.2	1.2 ± 0.2
L'_{line}[10^9 K km s^{-1}pc^{-2}]	<1.0	30.4 ± 0.7	4.1 ± 0.8

Table 2. Atomic fine structure line flux measurements from the line maps ($1.2\times$FWHM$_{\mathrm{CII}}=482\,\mathrm{km\,s^{-1}}$), flux–corrected by 1/0.84. Upper limits are given at the 3σ level. The first 3 lines give luminosity for the total integrated flux and the last 3 for the peak [C II]$_{158\,\mu\mathrm{m}}$ surface brightness. All fluxes are derived applying residual–scaling correction, and luminosities are computed following the definitions of Solomon et al. (1997)

for an additional broad component, which was reported in Maiolino et al. (2012) and Cicone et al. (2015) (with a peak flux density of up to $\sim10\,\mathrm{mJy}$ in the largest aperture of $r=4$”).

We note that, regardless of the aperture chosen or the use of residual scaling, a broad [C II]$_{158\,\mu\mathrm{m}}$ component is not recovered in our analysis (see Appendix D). We have checked that the continuum fluxes in the lower and higher frequency sidebands are consistent within $\sim2\%$. This ensures that the continuum of J1148+5251, determined from the full $\sim$ 7.6 GHz sideband, is consistent with that determined solely from the single $\sim$ 3.8 GHz baseband containing the [C II]$_{158\,\mu\mathrm{m}}$ line. We also show in Appendix E that the choice of the line masking width and the flux calibration differences between the two $\sim$ 3.8 GHz basebands do not impact the recovered [C II]$_{158\,\mu\mathrm{m}}$ line.

The presence of a broad [C II]$_{158\,\mu\mathrm{m}}$ wing in previous works (Maiolino et al. 2012; Cicone et al. 2015) and its absence in our data seems puzzling at first. Indeed Cicone et al. (2015) reach a sensitivity in the [C II]$_{158\,\mu\mathrm{m}}$ line comparable to ours ($0.46\,\mathrm{mJy\,beam^{-1}}$ vs. $0.45\,\mathrm{mJy\,beam^{-1}}$ per $100\,\mathrm{km\,s^{-1}}$ channel) and have similar angular resolution (1.3”$\times1.2$” vs. 1.89”$\times1.59$”). However, their observations were performed with a smaller number of antennas (6, i.e. 15 baselines, where the new observations were done with 8–9, i.e. 28–36 baselines), using a correlator that provided a spectral coverage ($\sim$ 3.6 GHz) twice as narrow than the new observations ($\sim$ 7.7 GHz) around the [C II]$_{158\,\mu\mathrm{m}}$ line. Hence the discrepancy cannot stem from sensitivity or resolution issues and we expect that due to our slightly

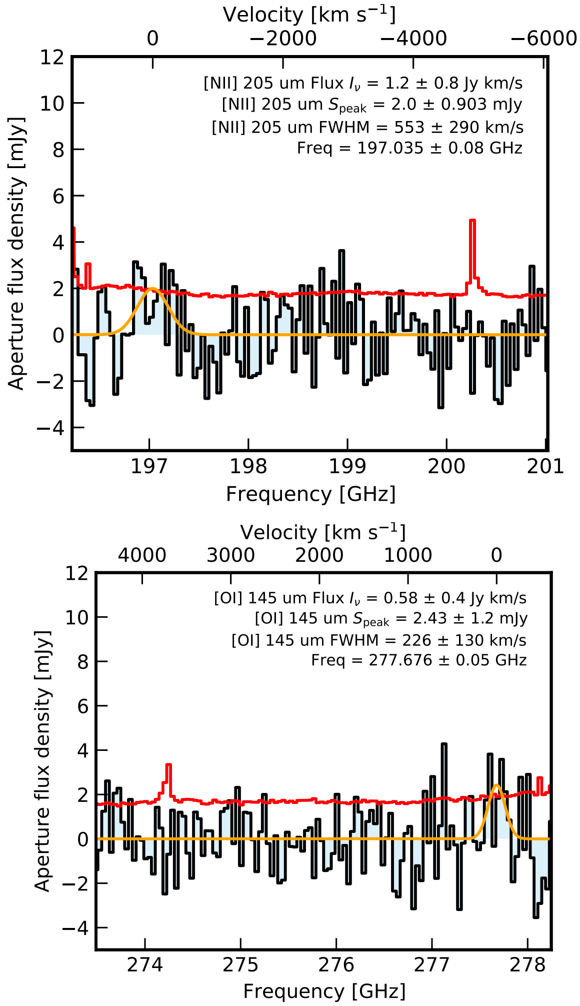

Figure 4. Continuum–subtracted spectrum of the [N II]$_{205\,\mu\rm m}$ (upper panel) and [O I]$_{146\,\mu\rm m}$ (lower panel). The spectra (black lines, shaded blue) are extracted in $r = 3$" aperture using residual scaling (see Sec. 2). The rms noise per channel for a $r = 3$" aperture is shown in red, and a single Gaussian fit is shown in orange (the best–fit parameters and uncertainties in the upper right corner).

larger beam, larger number of antennas and higher imaging fidelity we would be more sensitive, if anything, to extended [C II]$_{158\,\mu\rm m}$ structures in J1148+5251 compared to earlier data. The wider spectral coverage of the new *Polyfix* enables us to better constrain the dust continuum emission and the exact shape of a potential broad [C II]$_{158\,\mu\rm m}$ emission line.

We can only speculate that the most likely explanation for this discrepancy is related to the continuum subtraction. The previously available bandwidth ($\pm2000\,\rm km\,s^{-1}$), possibly compounded with effects at the edges of the band, could potentially complicate the definition of the exact continuum level, and may mimic broad [C II]$_{158\,\mu\rm m}$ emission filling the entire band. This would explain why the continuum flux densities at 259 GHz reported in both Maiolino et al. (2012) and Cicone et al. (2015) (3.7 mJy and 3.3 ± 0.7 mJy, respectively) are lower than our measurement (4.64 ± 0.26 mJy). An unsubtracted continuum flux density of ~ 1 mJy, integrated over $\pm1500\,\rm km\,s^{-1}$ would correspond to an integrated flux of $3\,\rm Jy\,km\,s^{-1}$, comparable to the broad [C II]$_{158\,\mu\rm m}$ line fluxes reported by Maiolino et al. (2012) and Cicone et al. (2015) for small apertures ($r \lesssim 3$").

4.2. *Spatially extended [C II]$_{158\,\mu\rm m}$ emission*

The [C II]$_{158\,\mu\rm m}$ emission is spatially extended (Fig. 3). In Figure 6 we show the dust and [C II]$_{158\,\mu\rm m}$ radial profiles to investigate their spatial extension. The dust continuum emission (at $\sim$ 259 GHz) is as extended (within 1σ errors) as the [C II]$_{158\,\mu\rm m}$ emission ($r \sim 2.5$", 3σ), suggesting that both trace the ISM of the galaxy rather than an extended [C II]$_{158\,\mu\rm m}$ halo or outflow (Figure 6, leftmost panel). This corresponds to a scale of $\sim$ 1.6" or $\sim$ 9 kpc once accounting for beam–convolution. This is twice larger than any of the 27 quasars observed in [C II]$_{158\,\mu\rm m}$ by Venemans et al. (2020), confirming earlier reports (Maiolino et al. 2012; Cicone et al. 2015) that J1148+5251 is an outlier in terms of [C II]$_{158\,\mu\rm m}$ emission extension. This result holds as well if the dust extension is measured from other spectral setups (e.g., Fig. 1).

The extension of [C II]$_{158\,\mu\rm m}$ is however asymmetric, with a prominent NE–SW axis (Fig. 3, although this is less pronounced with a larger channel width, see Fig. 8, first panel). In the second and third panel of Figure 6 we compare the dust continuum and the [C II]$_{158\,\mu\rm m}$ radial surface brightness profile for the radially averaged case, the NE–SW axis and the NW–SE axis (see Fig. 3). Whilst we find no evidence for an extended [C II]$_{158\,\mu\rm m}$ halo when radially averaging or on the NW–SE axis, along the NE–SW axis [C II]$_{158\,\mu\rm m}$ is significantly more extended than the dust continuum (5.8σ).

We finally explore the extension of the [C II]$_{158\,\mu\rm m}$ emission and the dust continuum directly in the *uv* plane. To that end, we use the UV_FIT and UV_CIRCLE routines in GILDAS/MAPPING to fit the visibilities with a point source and 2D Gaussian emission model, and then bin the modelled and observed visibilities radially. We plot the real part of the visibilities against the *uv* radius in Figure 7. In such plots, a point source gives a constant flux density at all *uv* radii, while a Gaussian emission model yields a Gaussian profile centered at $r = 0$. We find good agreement between the observed visibilities and a composite emission model comprising a point source and a 2D Gaussian. We fit both a circular Gaussian and an elliptical Gaussian

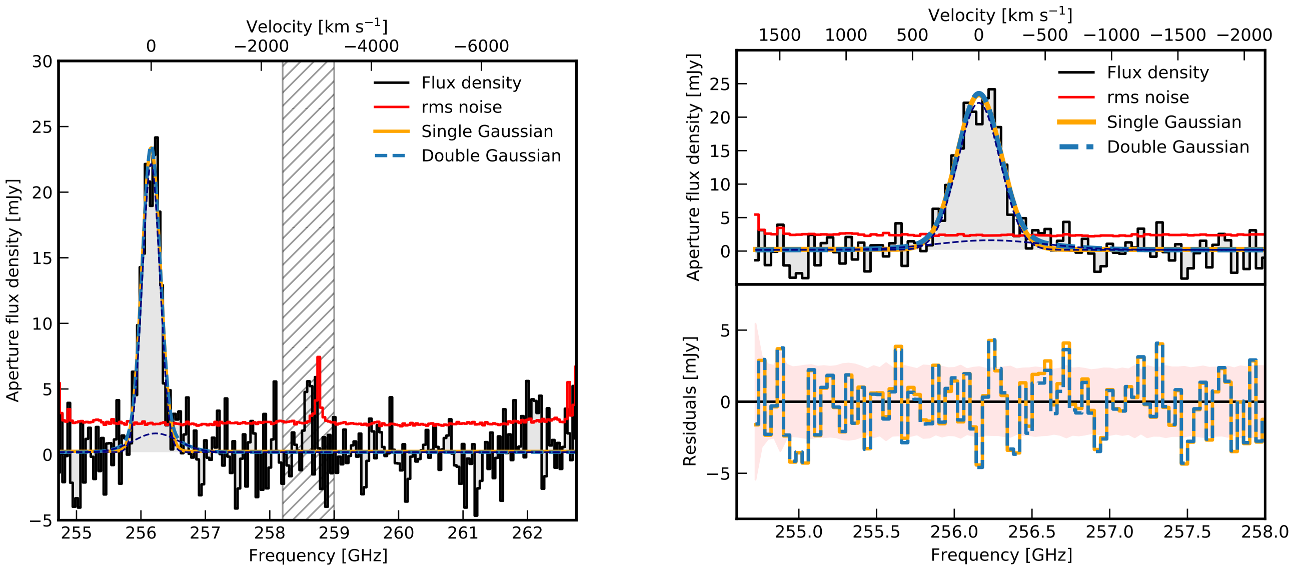

Figure 5. Continuum–subtracted spectrum of the [C II]$_{158\,\mu\mathrm{m}}$ line (black) extracted in a $r = 3$" aperture using residual scaling and 1– and 2–components Gaussian fits (orange line and dashed–dotted blue, respectively). Thin dashed dark blue lines show the two components of the double Gaussian model. Both models are fitted to the entire frequency range to the exception of the overlap between the two sidebands (hatched in grey). The right panels show a zoomed–in version of the right plot and the residuals of the two models. The shaded red are in the bottom right shows the noise level, computed using the rms noise in each channel in mJy beam^{-1}, and scaled accordingly for the number of beams in the $r = 3$" aperture. We find no evidence for a broad [C II]$_{158\,\mu\mathrm{m}}$ emission line in J1148+5251 (see text for details).

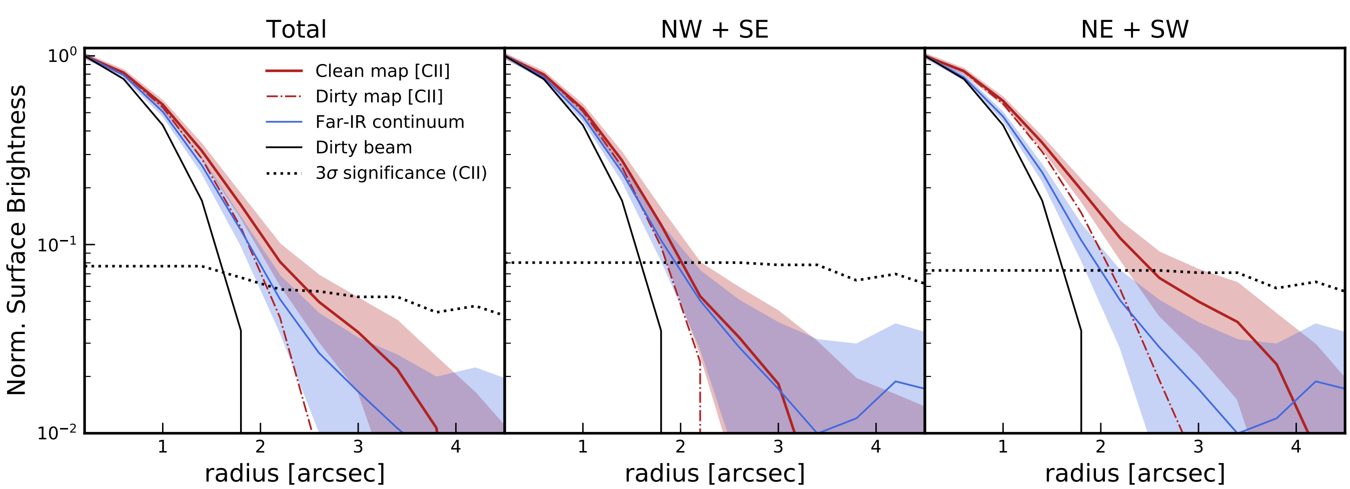

Figure 6. [C II]$_{158\,\mu m}$ (red) and dust continuum emission (blue) profiles for J1148+5251, which both extend up to ~ 2.5" (~ 14 kpc) at the 3σ level. The shaded areas show the corresponding 1 sigma errors. A point source profile is shown in black and the dirty (before cleaning and residual–scaling) profile is shown in dashed–dotted red. . The three panels show, the radial profile integrated, from left to right, over the full 2π, only in the North–West and South–East quadrant, and finally only in the North–East and South–East (e.g. along the extended emission seen in Figure 3). In the latter case, the [C II]$_{158\,\mu m}$ halo is more extended than the FIR continuum (5.8σ significance).

to the dust and [C II]$_{158\,\mu m}$ continuum visibilities. For the [C II]$_{158\,\mu m}$ emission, the best–fit model gives corrected velocity–integrated flux of $4.2 \pm 0.5\,\mathrm{Jy\,km\,s^{-1}}$ in the point source component, and $5.0 \pm 0.5\,\mathrm{Jy\,km\,s^{-1}}$ in the extended Gaussian, in good agreement with the flux derived from the line map (Table 2) and the fitted spectrum (see Appendix D). The elliptical Gaussian models yields velocity–integrated fluxes of $5.0 \pm 0.3\,\mathrm{Jy\,km\,s^{-1}}$ and $5.5 \pm 0.4\,\mathrm{Jy\,km\,s^{-1}}$ for the point source and resolved components, respectively. In either case, we are consistent with the large fraction of emission coming from the unresolved component reported in Cicone et al. (2015) but not with the overall flux, which is possibly due to continuum subtraction differences as discussed previously in Section 4.1. Additionally, the unresolved flux is consistent with that measured at higher resolution data (Walter et al. 2009a), suggesting the difference in total flux is due to the extended component being resolved out in high–resolution configurations.

The FWHM of the [C II]$_{158\,\mu m}$ Gaussian component is $r = 1.6" \pm 0.2"$ (9 ± 1 kpc), or $a = 3.6" \pm 0.3"$ (20 ± 2 kpc), b $= 1.8" \pm 0.2"$ (10 ± 1 kpc) for the elliptical model. This is in agreement with the scale of the 3σ extension directly measured on the cleaned image. The elliptical Gaussian has a major/minor axis difference and angle (PA=53±4 deg) in agreement with the asymmetric [C II]$_{158\,\mu m}$ emission discussed above. However, a likelihood ratio test does not prefer the elliptical Gaussian model over the circular one (p–value = 0.83, e.g. 0.96σ significance). We do not find any difference between the elliptical Gaussian and circular Gaussian model for the dust emission (see Fig. 7). The best–fit model for the dust emission gives a flux density of 1 ± 0.7 mJy and 3.3 ± 0.7 mJy for the unresolved/resolved components, with the sum in agreement with the measurement aperture–integrated flux density (Table 1). The dust uv profile (Fig. 7, bottom panel) does not show clear evidence for a flattening at large uv distances that is characteristic of a point source. The Gaussian component has a FWHM of $r = 0.7" \pm 0.1"$ (3.9 ± 0.6kpc).

Cicone et al. (2015) reported a complex velocity structure of the [C II]$_{158\,\mu m}$ outflow, with emission clumps detected up to ~ 30 kpc and $\sim 1000\,\mathrm{km\,s^{-1}}$ offsets from the central emission, particularly visible in an emission line map integrated over a $(-1400, 1200)\,\mathrm{km\,s^{-1}}$ interval. Such features are not recovered in our data when averaging over a similar velocity interval (Fig. 8, left). The [C II]$_{158\,\mu m}$ emission is concentrated mostly within ~ 11 kpc and no significant emission is recovered beyond 3” [7]. We further show in Appendix F that no significant velocity structure is detected in J1148+5251 in our data, neither by inspecting the channel maps (with channel width $\Delta v = 120\,\mathrm{km\,s^{-1}}$) nor by means of a kinematical analysis. We attribute the difference to previous work to NOEMA's improved image fidelity.

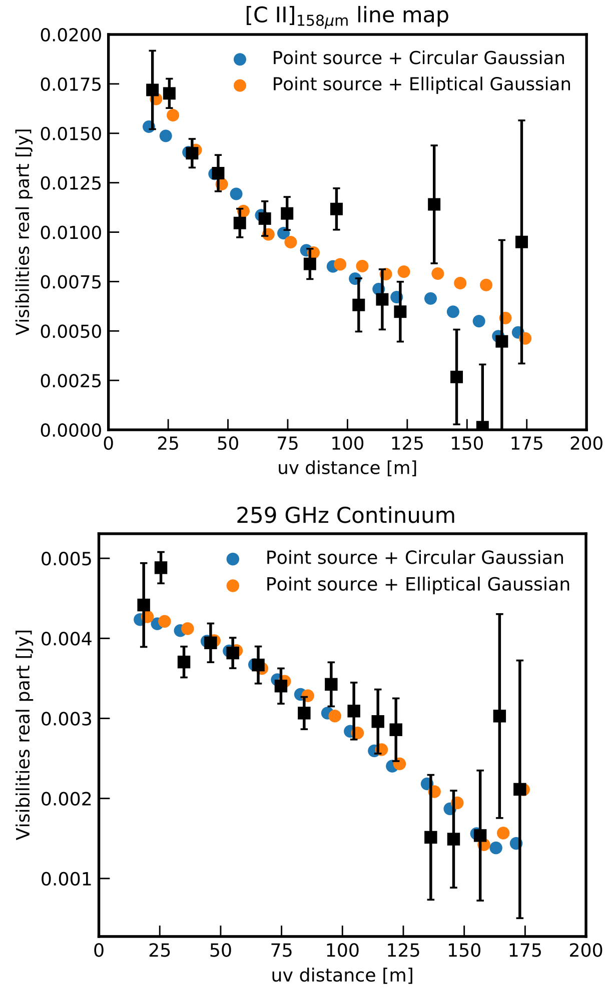

Figure 7. Observed (black) and modelled (blue,orange) real part of the visibilities for the [C II]$_{158\,\mu m}$ emission (integrated over $\Delta v = 482\mathrm{km\,s^{-1}}$) and dust continuum in J1148+5251. The model points are slightly offset for presentation purposes. The difference between the two models (blue: point source + circular Gaussian, orange: point source + elliptical Gaussian) is not statistically significant (p–value = 0.83, e.g. 0.96σ significance).

[7] Following the analysis of Cicone et al. (2015), we also plot the blue– and red–shifted component ($(-1500, -400)\,\mathrm{km\,s^{-1}}$ and $(+400, +1500)\,\mathrm{km\,s^{-1}}$) of the [C II]$_{158\,\mu m}$ emission, and find only marginal detections (3.7 and 3.9σ) which are not spatially offset (Fig. 8).

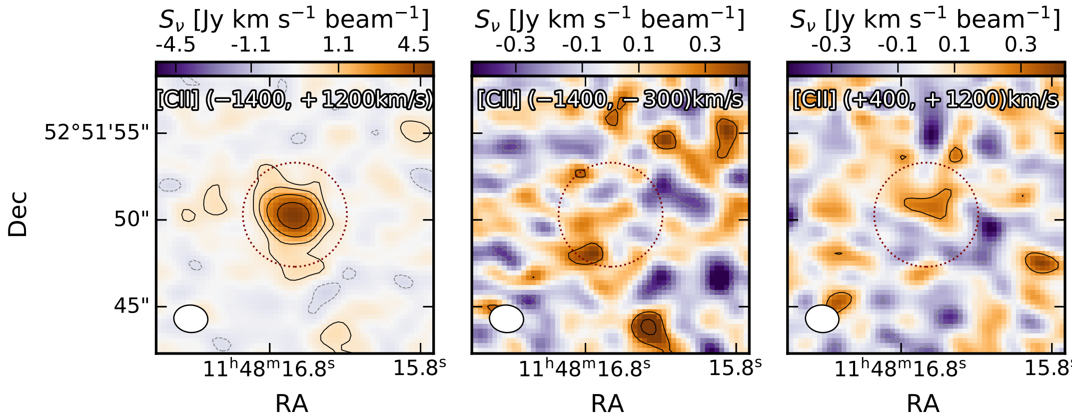

Figure 8. From left to right: map of the [C II]$_{158\,\mu\mathrm{m}}$ emission, averaged over the velocity ranges $(-1400, 1200)\,\mathrm{km\,s^{-1}}$, $(-1400, -300)\,\mathrm{km\,s^{-1}}$ and $(+400, +1200)\,\mathrm{km\,s^{-1}}$. These velocity ranges are similar to that presented in Cicone et al. (2015) who reported 6σ [C II]$_{158\,\mu\mathrm{m}}$ clumps at $2-4$ arcsec from the source center in the blue/red–shifted wings of the [C II]$_{158\,\mu\mathrm{m}}$ emission. Such spatially and spectrally offset emission is not recovered in our data. The 1σ rms values in the above three maps are $0.25, 0.16, 0.13\,\mathrm{mJy\,beam^{-1}}$ compared to $0.26, 0.17, 0.14\,\mathrm{mJy\,beam^{-1}}$ in Cicone et al. (2015). This figure shows contours in logarithmic increments (-4,-2,2,4,8,16,32)σ whereas Cicone et al. (2015) use linear 3σ steps.

.

5. ISM PROPERTIES

5.1. *[C II]$_{158\,\mu\mathrm{m}}$ emission*

In the following analysis, we adopt luminosities measured from the line maps. We measure a [C II]$_{158\,\mu\mathrm{m}}$ line–luminosity $L_{\text{[C II]}} = (10.6 \pm 0.5) \times 10^8 \mathrm{L}_\odot$ ($\mathrm{L}'_{\text{[C II]}} = (48.1 \pm 2.5) \times 10^9\,\mathrm{K\,km\,s^{-1}pc^{-2}}$). Following the [CII]–SFR relation of De Looze et al. (2014) for high–redshift ($z > 0.5$) galaxies, we find $\mathrm{SFR} = 2041 \pm 111\,\mathrm{M_\odot\,yr^{-1}}$, in good agreement with the SFR inferred from the continuum luminosities. Using the De Looze et al. (2014) calibration for AGNs does lower the result ($\mathrm{SFR} = 857 \pm 35\,\mathrm{M_\odot\,yr^{-1}}$), and that for ULIRGS increases the inferred SFR ($\mathrm{SFR} = 5562 \pm 257\,\mathrm{M_\odot\,yr^{-1}}$). This agreement between the [C II]$_{158\,\mu\mathrm{m}}$ and the infrared-luminosity based SFR is also observed in other high–redshift quasars (e.g., Venemans et al. 2020; Novak et al. 2019) where the FIR luminosity is smaller.

Following Weiß et al. (2003, 2005), in the optically thin limit, the total mass of ions X emitting photons with rest–frame frequency ν_{ij} stemming from a transition between the i and j levels can be derived from the observed luminosity as

$$M_X = m_X \frac{8\pi k \nu_{ij}^2}{hc^3 A_{ij}} Q(T_{\rm ex}) \frac{1}{g_i} e^{-T_{\rm ex}/T_i} L'_{[X_{i\to j}]} \qquad (1)$$

where k is the Boltzmann constant, c the speed of light, h the Plank constant, m_X is the mass of a single ion X, $Q(T_{\rm ex}) = \sum_i g_i e^{-T_i/T_{\rm ex}}$ is the partition function of the species, with g_i the statistical weight of level i, T_i the energy of (above–ground) level i, $T_{\rm ex}$ is the excitation temperature of the $i \to j$ transition, and $L'_{[X_{ij}]}$ is the observed integrated source brightness temperature of the line in $K\,\mathrm{km\,s^{-1}pc^{-2}}$. Note that Eq. 1 neglects heating from the CMB which is negligible for the the [O I]$_{146\,\mu m}$, [C II]$_{158\,\mu\mathrm{m}}$ and [N II]$_{205\,\mu\mathrm{m}}$ transitions, but not [C I]$_{370\mu\mathrm{m}}$ at $z \sim 6.4$. For C$^+$, Eq. 1 reduces to

$$M_{C^+}/M_\odot = 2.92 \times 10^{-4} Q(T_{\rm ex}) \frac{1}{4} e^{-91.2/T_{\rm ex}} L'_{\text{[C II]}} \qquad (2)$$

where $Q(T_{\rm ex}) = 2 + 4e^{91.2/T_{\rm ex}}$ is the [C II]$_{158\,\mu\mathrm{m}}$ partition function. The optically thin limit assumption, while widespread in the literature, is uncertain at higher–redshift since optical depths measurements, although pointing to moderate values, are scarce (e.g., Neri et al. 2014; Gullberg et al. 2015). Lagache et al. (2018) and Vallini et al. (2015) note that in the optically thick limit, only emission from PDRs would reach the observer. As we will show in Section 5.4, most of the [C II]$_{158\,\mu\mathrm{m}}$ emission in J1148+5251 comes indeed from PDRs, and hence we do no expect the optically thin limit assumption to affect our results. Assuming an excitation temperature $T_{\rm ex} = 50$K (from the CO modelling, Riechers et al. 2009), we find $M_{C^+} = (5.8 \pm 0.3) \times 10^7 M_\odot$. This is five times the neutral carbon mass ($M_C = 1.1 \times 10^7 M_\odot$) measured by Riechers et al. (2009).

5.2. *[N II]$_{205\,\mu\mathrm{m}}$ emission*

We report a [N II]$_{205\,\mu\mathrm{m}}$ marginal detection in J1148+5251 at SNR= 3.7 and an integrated ($r = 3$”) luminosity $L_{[NII]} = (0.4 \pm 0.2) \times 10^9 L_\odot$. This is in slight tension with the 3σ limit ($< 0.4 \times 10^9 L_\odot$) reported by Walter et al. (2009b) using the IRAM 30m telescope. Nonetheless, we would expect better image fidelity with the new NOEMA facility. We consider the [N II]$_{205\,\mu\mathrm{m}}$ detection marginal (3.7σ) and urge caution in interpretations that rely upon it.

The marginal (1.59" $\sim$ 1 beam) offset between [N II]$_{205\,\mu\mathrm{m}}$ and [C II]$_{158\,\mu\mathrm{m}}$ in J1148+5251 could be of interest. On the on hand, spatial offsets between low and high–ionization lines have been reported in other high–redshift quasars, most often between [C II]$_{158\,\mu\mathrm{m}}$ and [O III]$_{88\,\mu\mathrm{m}}$ (e.g., Novak et al. 2019). Spatial offsets have also been predicted in theoretical simulations (Katz et al. 2017, 2019) where they arise from different gas phases with different temperatures and densities. Although nitrogen and carbon have a similar ionization level, Katz et al. (2019) show that the [N II]$_{205\,\mu\mathrm{m}}$ and [C II]$_{158\,\mu\mathrm{m}}$ can arise from different gas phases, with [C II]$_{158\,\mu\mathrm{m}}$ originating in lower temperature and higher density regions[8], which could explain the offset of [N II]$_{205\,\mu\mathrm{m}}$ towards the outskirts of J1148+5251. On the other hand, offsets often seen at low–resolution in high–redshift galaxies can disappear in higher–resolution data once fainter emission components are detected (e.g. see HZ10 in Pavesi et al. 2016, 2019). Following Ferkinhoff et al. (2010, 2011), we derive the minimum H^+ for the [N II]$_{205\,\mu\mathrm{m}}$ luminosity observed. To do so, we assume high densities and a high temperature (as found around O and B stars), such that all nitrogen in the HII regions is ionized. We use Eq. 1 to derive the mass of N^+ in J1148+5251 from the observed luminosity, with $\mathrm{A}_{10} = 2.1 \times 10^{-6}$ the Einstein coefficient of the ${}^3P_1 \rightarrow {}^3P_0$ transition, $g_1 = 3$ the statistical weight of the ${}^3P_1$ emitting level, $\nu_{10} = 1461.1\,\mathrm{GHz}$ the rest–frame frequency, and $g_t \simeq 9$ the partition function. We can then derive the minimum H^+ mass by assuming the upper limit on the ionized nitrogen to ionized hydrogen ratio (i.e. $\chi(N^+) = N^+/H^+$) to be the total nitrogen abundance ratio $\chi(N)$, such that

$$M(H^+) \geq M_{N^+} \frac{m_N}{m_H \chi(N^+)} = \frac{L_{[NII]205\mu m}}{\frac{g_1}{g_t} A_{10} h \nu_{10}} \frac{m_H}{\chi(N^+)} \quad , \tag{3}$$

We adopt the abundance value for HII regions $\xi(N) = 9.3 \times 10^{-5}$ from (Savage & Sembach 1996). Hence we estimate an ionized hydrogen mass $M(H^+) \geq (2.1 \pm 1.0) \times 10^9 M_\odot (2\sigma$ level). Using the H_2 gas mass from the CO luminosity (Riechers et al. 2009), the ionized–to–molecular gas ratio is $M(H^+)/M(H_2) > 0.1$. This is significantly higher than what is found by Ferkinhoff et al. (2011) (using a compilation by Brauher et al. (2008)) for local galaxies using the [NII] 122 μm line (< 0.01). We caution here again that the [N II]$_{205\,\mu\mathrm{m}}$ line is marginal.

The [CII]/FIR ratio (so–called [C II]$_{158\,\mu\mathrm{m}}$ deficit" , $\simeq (7.8 \pm 1.3) \times 10^{-4}$), [NII]/FIR ratio ([N II]$_{205\,\mu\mathrm{m}}$ deficit" ,$\sim (2.9 \pm 1.5) \times 10^{-5}$) and dust temperature ($53 \pm 8$ K) are all in agreement with the ratio trends (extrapolated to high temperature observed in J1148+5251) observed in local ULIRGS (Díaz-Santos et al. 2017) and high–redshift galaxies or quasars (Pavesi et al. 2019; De Breuck et al. 2019; Novak et al. 2019; Li et al. 2020; Pensabene et al. 2021, see Figure 9). We note that the [CII]/[NII] luminosity ratio (10.6 ± 3.7) is slightly low for dense PDRs/XDRs regions expected around high–redshift quasars (e.g., Decarli et al. 2014; Pavesi et al. 2019), though the uncertainties are large given the marginal detection in the [N II]$_{205\,\mu\mathrm{m}}$ line. Finally, we also test Zhao et al. (2016) [N II]$_{205\,\mu\mathrm{m}}$–SFR scaling relation derived from local ULIRGS which gives $\mathrm{SFR} = 794 \pm 274\ \mathrm{M}_\odot\,\mathrm{yr}^{-1}$, lower than the [C II]$_{158\,\mu\mathrm{m}}$ and FIR-derived values.

5.3. *[O I]$_{146\,\mu\mathrm{m}}$ emission*

The peak of the [O I]$_{146\,\mu\mathrm{m}}$ emission is located at the same position as the [C II]$_{158\,\mu\mathrm{m}}$ emission. The [O I]$_{146\,\mu\mathrm{m}}$/FIR ratio is 1.3×10^{-5} in good agreement with that of local ULIRGS with comparable FIR surface flux density (Herrera-Camus et al. 2018). Using again Eq. 1 for the [O I]$_{146\,\mu\mathrm{m}}$ ${}^3P_0 \rightarrow {}^3P_1$ transition ($T_0 = 329$ K, $g_0 = 1$, $Q(T_{\mathrm{ex}}) = 5 + 3e^{-329/T_{\mathrm{ex}}} + e^{-228/T_{\mathrm{ex}}}$), we derive a neutral oxygen mass

$$M_O/M_\odot = 6.19 \times 10^{-5} Q(T_{\mathrm{ex}}) e^{329/T_{\mathrm{ex}}} L'_{[OI]} \quad . \tag{4}$$

Assuming an excitation temperature $T_{\mathrm{ex}} = 50\,\mathrm{K}$ (from the CO modelling, Riechers et al. 2009), we find $M_O = (9 \pm 5) \times 10^8 M_\odot$. This estimate is extremely sensitive on the excitation temperature, e.g. ranging from $0.7 \times 10^7 M_\odot$ at 200 K to $8 \times 10^8 M_\odot$ at $T_{\mathrm{ex}} = 50K$. Note that the above expression only applies in the optically thin limit which is probably not the case of [O I]$_{146\,\mu\mathrm{m}}$, therefore underestimating the neutral oxygen mass.

5.4. *CLOUDY modelling of the fine–structure line ratios*

We now use the FSL ratios to determine the physical properties of the ISM of J1148+5251. In order to do so, we make use of CLOUDY (Ferland et al. 2017), a spectral synthesis code designed to simulate the spectra of astrophysical plasmas used to study both low and high redshift galaxies sub–mm lines. The grid of models used in this work were generated to study both high–redshift quasar hosts and their companions in Pensabene et al. (2021), which we refer to for further details. To

[8] Although a minor fraction of [C II]$_{158\,\mu\mathrm{m}}$ traces the same H II regions as [N II]$_{205\,\mu\mathrm{m}}$, see Sec 5.4.

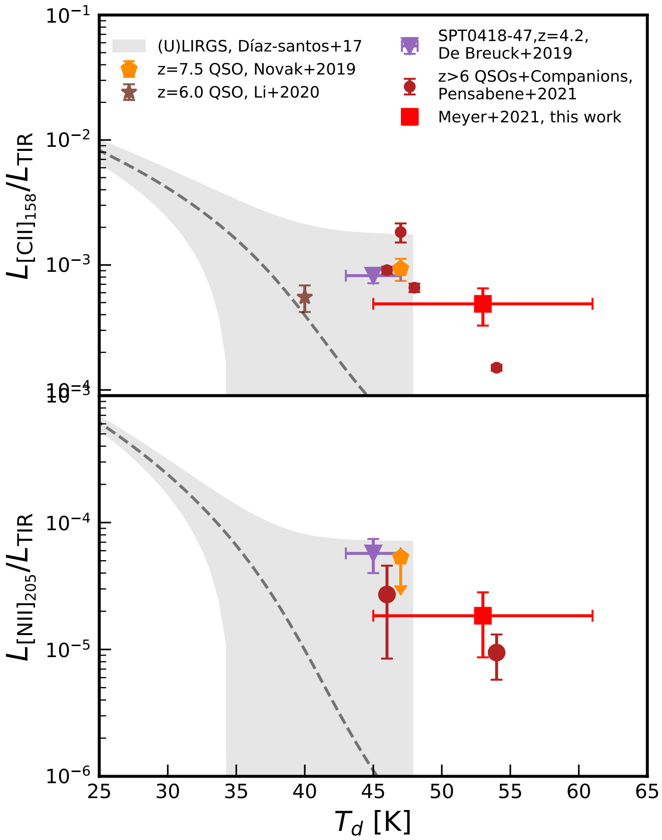

Figure 9. [C II]$_{158\,\mu m}$ and [N II]$_{205\,\mu m}$ line deficits of local (U)LIRGS (shaded grey Díaz-Santos et al. 2017), high–redshift galaxy SPT0418–47 (purple triangle De Breuck et al. 2019), and high–redshift quasars (orange pentagon, dark orange star, dark red circles Novak et al. 2019; Li et al. 2020; Pensabene et al. 2021, respectively) and companion galaxies (dark red circles Pensabene et al. 2021). Our measurements for J1148+5251 are shown in red.

summarise briefly, the model grids includes both PDR and XDR predictions for total hydrogen column densities $N_{\rm H}/[{\rm cm}^{-2}] = 10^{23} - 10^{24}$, total hydrogen number density $1 < \log n/[{\rm cm}^{-3}] < 6$, and local FUV radiation field $2 < \log G/[G_0] < 6$ in units of Habing flux (for the PDRs) or X-ray flux $-2 < \log F_X/[{\rm ergs}^{-1}\,{\rm cm}^{-2} < 2] < 2$ (for the XDRs). For each combination of parameters, the flux of various lines of interest is predicted and the ISM conditions can be determined by comparing to the observed line ratios.

Whereas [C II]$_{158\,\mu m}$ can originate from both the neutral and ionized gas phase, [O I]$_{146\,\mu m}$ and [C I]$_{370\mu m}$ originates solely in the neutral gas phase/PDRs. It is therefore crucial to determine which fraction of the [C II]$_{158\,\mu m}$ emission in J1148+5251 comes from the neutral gas. [N II]$_{205\,\mu m}$ and [C II]$_{158\,\mu m}$ have very close critical density in ionized media, therefore the [C II]$_{158\,\mu m}$–to–[N II]$_{205\,\mu m}$ ratio is primarily a function of the N$^+$/C$^+$ abundance ratio. (e.g., Oberst et al. 2006). Photoionization models (e.g., Oberst et al. 2006; Pavesi et al. 2016; Croxall et al. 2017) predict a relatively constant ratio $(2.5-3)$ for [N II]$_{205\,\mu m}$/[CII]$^{\rm ion}_{158\mu m}$ for a large range of electron density. For consistency with the existing literature, we adopt [N II]$_{205\,\mu m}$/[CII]$^{\rm ion}_{158\mu m} = 3$. Any deviation from that ratio can be interpreted as [C II]$_{158\,\mu m}$ emission from the neutral phase. The fraction of [C II]$_{158\,\mu m}$ emission originating in the neutral phase is therefore

$$f([{\rm CII}], {\rm neutral}) \simeq 1 - 3\frac{{\rm L}_{[{\rm NII}]_{205\mu m}}}{{\rm L}_{[{\rm CII}]_{158\,\mu m}}} \quad . \qquad (5)$$

The ratio of the luminosities measured in this work for J1148+5251 is 27 ± 13 for the aperture–integrated ($r = 3$") flux and $> 100 (2\sigma\,{\rm level})$ at the peak of the [C II]$_{158\,\mu m}$ emission. In either case, most of the [C II]$_{158\,\mu m}$ emission (88% – 97%) comes from the neutral phase.

Given the resolution of our data, we use the $r = 3$" aperture–integrated line luminosities to compute line luminosity ratios and compare to the grid of CLOUDY models. In order to include properly the [C I]$_{370\mu m}$ measurements from Riechers et al. (2009), we have repeated the line map procedure detailed in Section 2 on the original [C I]$_{370\mu m}$ data. We produce a line map with width $\Delta v = 482\,{\rm km\,s}^{-1}$ and integrate the flux up to $r = 3$", finding $S_{[CI]369}\Delta v = 0.45 \pm 0.16\,{\rm Jy\,km\,s}^{-1}$ and a line luminosity $L_{[CI]369} = (0.2 \pm 0.08) \times 10^9 L_\odot$. We show in Figure 10 the radiation field and density predictions of CLOUDY for the observed FSL ratios. We find that the different line ratios are not perfectly reproduced for a single density and radiation field in the chosen grid of models. However, the [C II]$_{158\,\mu m}{}^{\rm neutral}$ / [C I]$_{370\mu m}$ luminosity ratio (47 ± 3) excludes XDR models which cannot reproduce such high ratios (the maximum being ~ 15) (e.g., Venemans et al. 2017a,b; Novak et al. 2019; Pensabene et al. 2021). We note that this result, based on the analysis of the fine structure lines, is in tension with Gallerani et al. (2014) who concluded that an XDR component is needed in J1148+5251 to explain their reported CO(17-16) line. However, as noted by the authors, this line is potentially contaminated by the nearby OH$^+$ emission, and thus additional observations of high–J CO lines are needed to clarify the situation.

The PDR models in agreement with the observed ratios (except [O I]$_{146\,\mu m}$/ [C I]$_{370\mu m}$) have an HI column density of $N_{HI} = 10^{23}{\rm cm}^{-2}$, high radiation fields ($10^{3.5-4.5}\,G_0$) and moderate hydrogen number densities ($n \simeq 10^{3.5-4.5}\,{\rm cm}^{-3}$), commensurable with other studies of high–redshift quasars (e.g., Novak et al. 2019; Pensabene et al. 2021). The model grids do not repro-

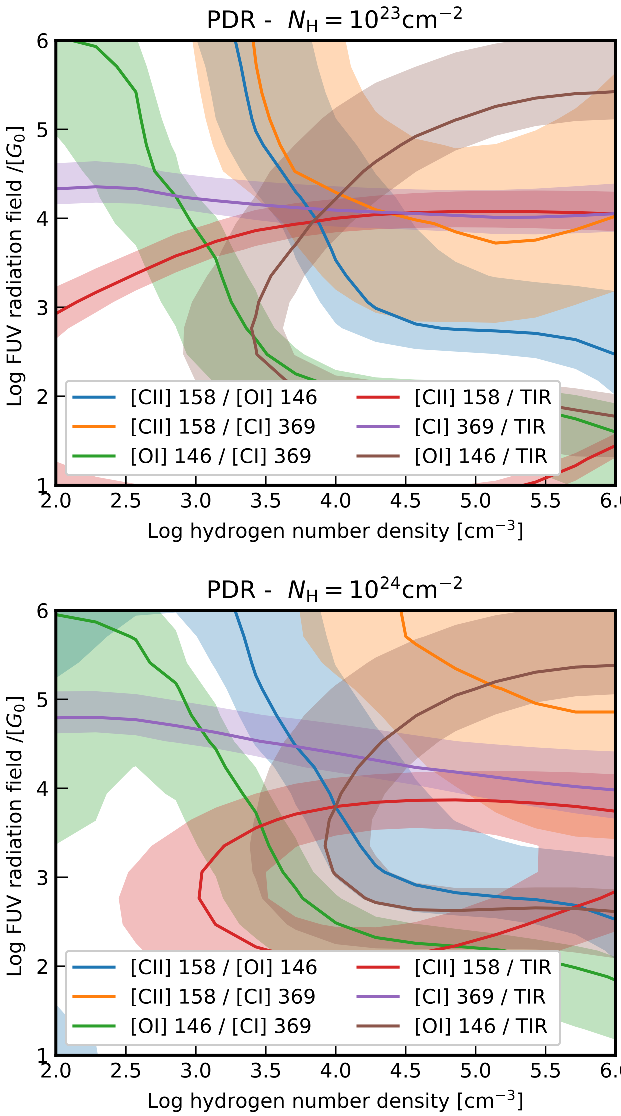

Figure 10. ISM constraints from the FSL ratios predicted by CLOUDY. The observed ratio constraints from the aperture integrated fluxes are plotted in solid lines and the $\pm1\sigma$ values in shaded area of the same color.

duce the observed [N II]$_{205\,\mu m}$/[C II]$_{158\,\mu m}$ ratio since it was not created to model the ionized phase (HII regions) traced by [N II]$_{205\,\mu m}$ emission. The [O I]$_{146\,\mu m}$/ [C I]$_{370\mu m}$discrepancy could stem from the different quality and resolution of the data, as well as the low SNR of both lines. Deeper and higher resolution of the inner and outer [C II]$_{158\,\mu m}$ emitting regions, combined the presence or absence of [O I]$_{146\,\mu m}$, [N II]$_{205\,\mu m}$ and [C I]$_{370\mu m}$, would be required to further investigate the ISM of J1148+5251.

6. CONCLUSIONS

We report new NOEMA observations of the z=6.42 quasar J1148+5251 in the atomic fine structure lines of [C II]$_{158\,\mu m}$, [O I]$_{146\,\mu m}$ and [N II]$_{205\,\mu m}$ and the underlying dust continuum emission. The high–fidelity data, together with the large instantaneous bandwidths that NOEMA provides, enabled us to revisit the properties of the quasar's host galaxy and derive the physical conditions of its interstellar medium. The main conclusions of this paper are as follows:

- The [C II]$_{158\,\mu m}$ line profile can be fitted with a single Gaussian with a FWHM of 385 km s^{-1}. The new data do not show evidence for the presence of broad [C II]$_{158\,\mu m}$ wings extending to $\sim$ 1300 km s^{-1} or for [C II]$_{158\,\mu m}$ clumps $\sim 10-15$ kpc away from the quasars position (cf. Maiolino et al. 2012; Cicone et al. 2015). We speculate that these discrepancies could stem from possible issues related to the continuum subtraction in the earlier studies, which are now alleviated thanks to the wider spectral coverage of the new NOEMA Polyfix correlator and better uv–coverage due to additional antennas.

- A *uv* plane analysis confirms the presence of a extended [C II]$_{158\,\mu m}$ emission component (FWHM $\sim$ 1.6", 9 kpc) accounting for $\sim 50-60\%$ of the total [C II]$_{158\,\mu m}$ and most of the dust emission, in agreement with earlier studies (Maiolino et al. 2012; Cicone et al. 2015). J1148+5251 thus remains an outlier with very extended [C II]$_{158\,\mu m}$ and dust emission compared to other $z > 6$ quasars (e.g., Venemans et al. 2020).

- We find no evidence for an extended [C II]$_{158\,\mu m}$ halo beyond the dust continuum emission when averaging the [C II]$_{158\,\mu m}$ and dust profile radially. However, if the [C II]$_{158\,\mu m}$ emission is examined only along its NE–SW axis, a significant (5.8σ) excess [C II]$_{158\,\mu m}$ emission (w.r.t. to the dust) is detected up to $\sim$ 2.5", corresponding to $\sim$ 14 physical kpc ($\sim$ 9 kpc accounting for the beam size).

- We report the detection of [O I]$_{146\,\mu m}$ and [N II]$_{205\,\mu m}$ (tentatively) in J1148+5251. Using various empirical relations, we report a C^+ mass of $M_{C^+} = (2.7 \pm 0.1) \times 10^7 M_\odot$, an oxygen mass of $M_O = (12 \pm 4) \times 10^8 M_\odot$, and a lower limit on the ionized hydrogen mass $M_{H^+} > (4.6 \pm 0.16) \times 10^8 M_\odot (2\sigma\,\text{level})$.

- The FSL line ratios are consistent with the trends observed in local (U)LIRGs. We find that a large fraction ($\sim$ 90%) of the [C II]$_{158\,\mu m}$ emission originates in the neutral phase (PDR) of the gas.

- We have compared CLOUDY models to the observed FSL ratios in J1148+5251. The [C II]$_{158\,\mu\mathrm{m}}$/[C I]$_{370\mu\mathrm{m}}$ ratio excludes XDR models in favour of PDRs. We find good agreement for models that have a high radiation field ($10^{3.5-4.5}\,G_0$), a moderate hydrogen number densities ($n \simeq 10^{3.5-4.5}\,\mathrm{cm}^{-3}$) and HI column density $N_{HI} = 10^{23}\mathrm{cm}^{-2}$.

The results described here highlight the importance of large instantaneous bandwidths when observing high–redshift quasars (or galaxies) to search for weak extended emission of atomic or molecular lines. Our findings enabled a renewed view on the host galaxy of the J1148+5251 quasar shedding light on the feedback activity and providing new constraints on the excitation conditions of its interstellar medium that appear similar to what is found in local ULIRGs. Higher angular resolution and sensitivity data, in particular in the [C I]$_{370\mu\mathrm{m}}$ emission line, would be required to put additional constraints on the gas density and the ionisation source of J1148+5251 and further explore its properties.

ACKNOWLEDGMENTS

R.A.M., F.W., M.N. acknowledge support from the ERC Advanced Grant 740246 (Cosmic_Gas). D.R. acknowledges support from the National Science Foundation under grant Nos. AST–1614213 and AST–1910107. D.R. also acknowledges support from the Alexander von Humboldt Foundation through a Humboldt Research Fellowship for Experienced Researchers. This work is based on observations carried out with the IRAM NOrthern Extended Millimeter Array (NOEMA). IRAM is supported by INSU/CNRS (France),MPG(Germany), and IGN (Spain). The authors would like to thank wholeheartedly the staff at IRAM for their help with the reduction and analysis software GILDAS; and in particular M. Krips, V. de Souza, C. Herrera and J.-M. Winters.

Facilities: NOEMA (IRAM)

Software: astropy (The Astropy Collaboration et al. 2018), CLOUDY (Ferland et al. 2017), Numpy (Harris et al. 2020), Scipy (Virtanen et al. 2020), Matplotlib (Hunter 2007), Interferopy (https://github.com/mladenovak/interferopy)

APPENDIX

A. CURVE OF GROWTH ANALYSIS

In this appendix, we investigate what is the size of the aperture that is necessary to recover most of the continuum or [C II]$_{158\,\mu\mathrm{m}}$ line fluxes. Figure 11 shows the line flux density of [C II]$_{158\,\mu\mathrm{m}}$, [O I]$_{146\,\mu\mathrm{m}}$ and [N II]$_{205\,\mu\mathrm{m}}$ as well as the continuum flux density as a function of increasing aperture radius. We find that all line/continuum fluxes reach a maximum or plateau at an aperture radius $r = 3$", which corresponds to 16.9 kpc at $z = 6.42$. The [C II]$_{158\,\mu\mathrm{m}}$ flux presents tentative evidence for additional flux up to 4" ($\sim 1\,\mathrm{Jy\,km\,s^{-1}}$), but this is within the 1σ errors. Note that at large radii where there is no more cleaned flux, residual-scaling can become numerically unstable. Throughout this paper, an aperture of $r = 3$" is therefore adopted for measurements unless specified otherwise.

B. MULTISCALE AND HÖGBOM CLEANING METHODS

In this appendix, we briefly detail our experiments with different cleaning methods for our interferometric data. Högbom cleaning (Högbom 1974) is one of the standard method for cleaning interferometric data. It relies on iteratively finding peaks in the data and subtracting the dirty beam at that location until the residuals reach a desired level. It is particularly efficient for point sources, but struggles with large–scale emission which it tries to reconstruct using a multitude of point sources. In that case, so–called multi–scale algorithms which convolve the beam with various Gaussians to subtract larger scales are preferable (e.g., Wakker & Schwarz 1988).

Figure 12 shows the clean map, dirty map and residuals for Högbom and Multiscale clean on the [C II]$_{158\,\mu\mathrm{m}}$ map (integrated over $482\,\mathrm{km\,s^{-1}}$). Clearly, the Högbom clean residuals show a flat excess of 2σ flux filling the 3" aperture which would not be expected if the source was a single (or a limited number of) point source(s). On the contrary, the residuals of the Multiscale algorithm are closer to zero on average. Therefore, we chose the Multiscale algorithm for all [C II]$_{158\,\mu\mathrm{m}}$–derived quantities and images in this paper.

Figure 13 shows the clean, dirty and residual maps for the continuum maps and the other FSL maps for a Högbom clean. For the lower frequency continuum maps, [O I]$_{146\,\mu\mathrm{m}}$, and [N II]$_{205\,\mu\mathrm{m}}$ maps expect the residuals are well–

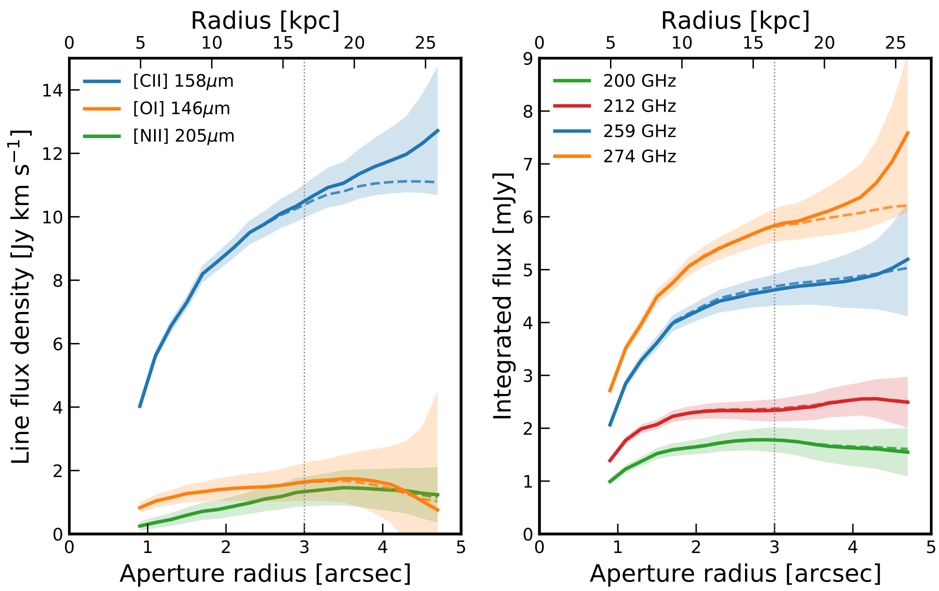

Figure 11. Fine–structure line flux densities (left panel) and integrated continuum flux (right panel) as a function of aperture radius. The solid and dashed lines show the fluxes with and without residual scaling correction (see Sec. 2). The final aperture radius of 3" was chosen to encompass all of the [C II]$_{158\,\mu m}$ emission and the continuum at the higher frequencies.

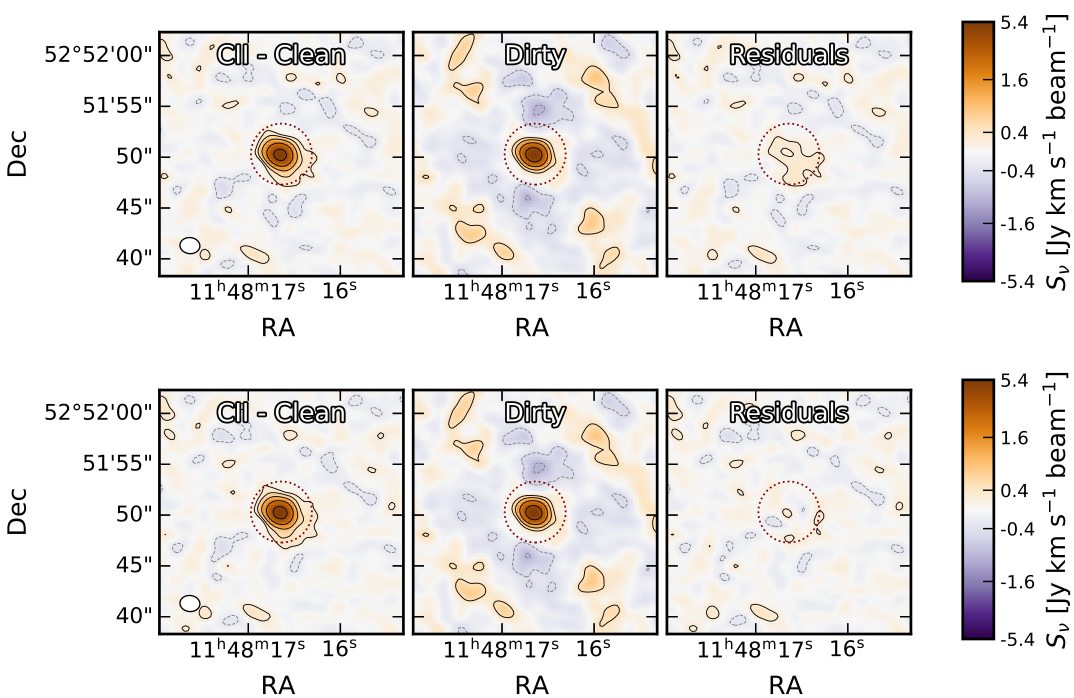

Figure 12. Clean, dirty and residual maps of the [C II]$_{158\,\mu m}$ emission for two different cleaning algorithms: Högbom (first row) and Multiscale (second row). Both are cleaned down to 2σ, where σ is the RMS noise of the dirty map.

behaved and do not require the use of multiscale cleaning. For the 259, 274 GHz continuum, some residuals are seen and the multiscale algorithm is adopted for those in the paper, albeit changing only the final continuum flux by $\lesssim 2\%$.

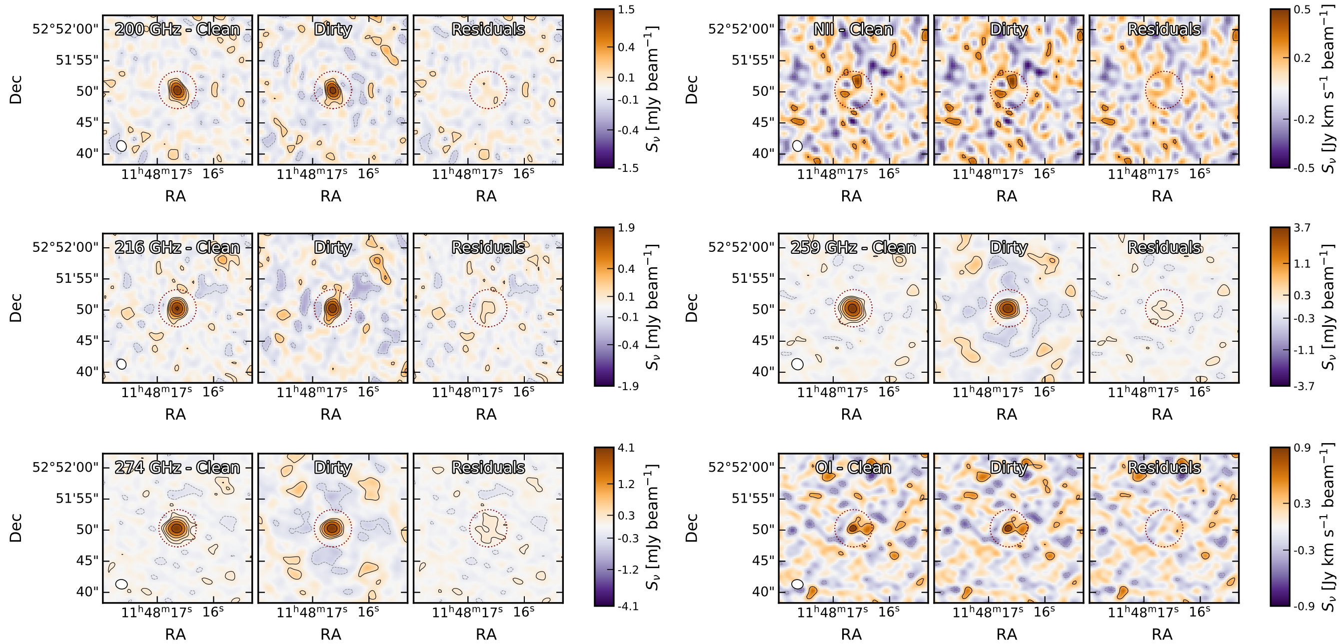

Figure 13. Clean,dirty and residual maps for a Högbom clean to 2σ of the 200 GHz continuum, emission, $216, 259, 274$ GHz continuum and finally [O I]$_{146\,\mu\mathrm{m}}$ emission.

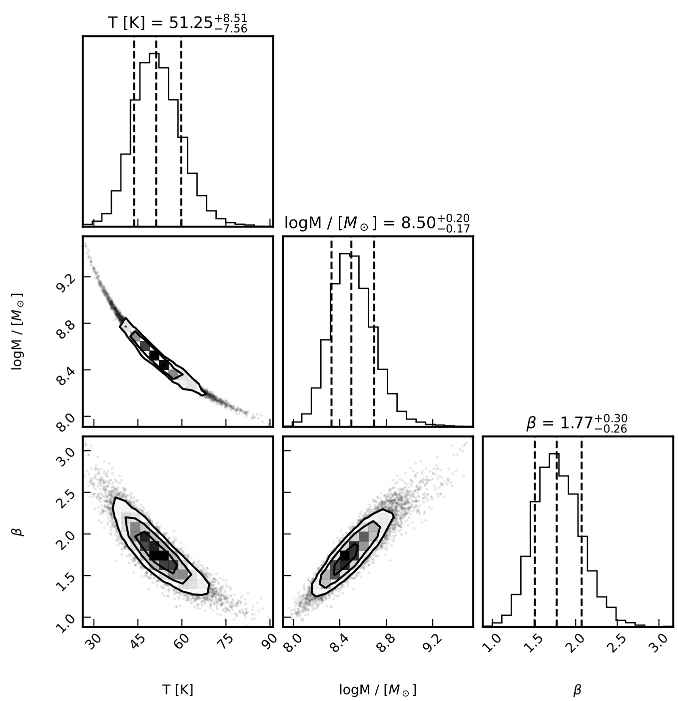

Figure 14. Dust SED fitting posterior distribution of the dust temperature T, dust mass M and the dust spectral emissivity index β.

C. DUST SED PARAMETER POSTERIOR DISTRIBUTION

We present in Figure 14 the posterior distribution of the dust SED parameters fitted in Section 2. The median dust properties derived are consistent with the existing literature on high–redshift quasars (e.g. Venemans et al. 2020).

	$r = 1$"		$r = 2$"		$r = 3$"		$r = 4$"	
	C15	This work	C15	This work	M12	This work	C15	This work
σ_v [km s^{-1}]	146 ± 11	158 ± 6	148 ± 16	162 ± 4	150 ± 20	171 ± 10	150 ± 20	175 ± 16
$S_{\rm peak}$ [mJy]	14.5 ± 0.9	9.41 ± 0.32	30 ± 3	20.1 ± 0.7	23 ± 2	23.5 ± 1.2	34 ± 4	24.7 ± 2.0
I_ν [Jy km s^{-1}]	5.3 ± 0.5	3.7 ± 0.2	11.0 ± 1.5	8.1 ± 0.4	14 ± 3	10.0 ± 0.8	13 ± 3	11.0 ± 1.0

Table 3. [C II]$_{158\,\mu\rm m}$ line fluxes measured from a Gaussian fit the aperture–integrated spectra in this work and previous studies. For aperture radius and study, we give the best–fit velocity width σ_v, the peak line flux density S_{peak} and the integrated flux I_ν. For the Cicone et al. (2015, C15) values, only the narrow component results ([C II]$_{158\,\mu\rm m}$ emission integrated between $(-200, 200)\,\rm km\,s^{-1}$) are reported. The Walter et al. (2009a) best–fit values are: $\sigma_v = 122 \pm 12\,\rm km\,s^{-1}$, $S_{\rm peak} = 12.7 \pm 1.1\,\rm mJy$, $I_\nu = 3.9 \pm 0.3\,\rm Jy\,km\,s^{-1}$. Similarly, the Maiolino et al. (2005) IRAM 30m measurement gives: $\sigma_v = 149 \pm 21\,\rm km\,s^{-1}$, $S_{\rm peak} = 11.8\,\rm mJy$, $I_\nu = 4.1 \pm 0.5\,\rm Jy\,km\,s^{-1}$.

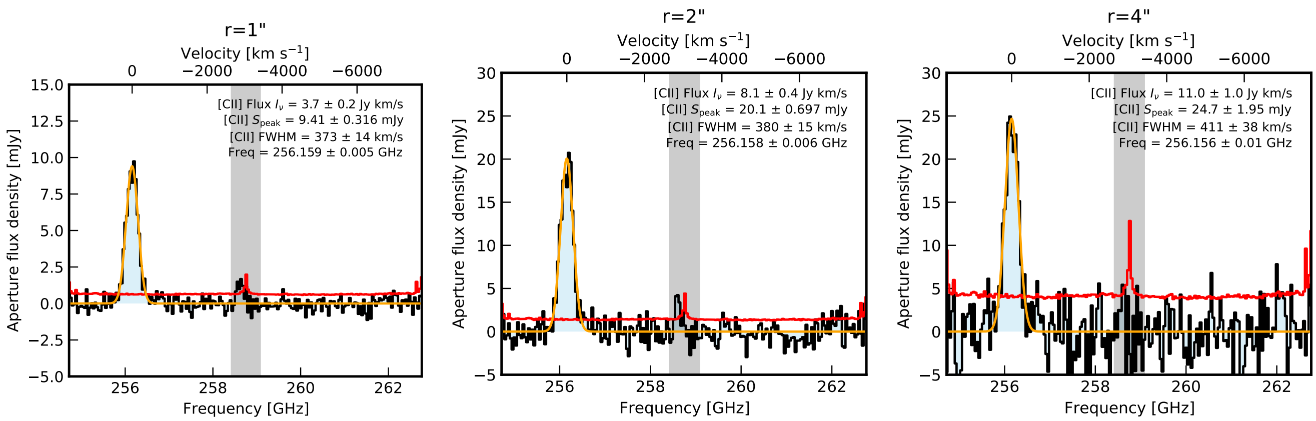

Figure 15. Continuum–subtracted aperture–integrated [C II]$_{158\,\mu\rm m}$ spectra (black) for circular aperture with radii $r = 1", 2", 4"$ as well as a central–pixel spectrum. The best fit Gaussian is shown in orange and the best–fit parameters are displayed in the upper–right corner of each plot.

D. [C II]$_{158\,\mu\rm m}$ FLUX DENSITY

In table 3, we compare the [C II]$_{158\,\mu\rm m}$ fluxes measured from the extracted aperture–integrated [C II]$_{158\,\mu\rm m}$ spectra for various aperture sizes between previous studies and this work. This work's spectra and best–fit Gaussians are displayed in Figure 15 for circular apertures with radii $r = 1", 2", 4"$ and a central–pixel–only spectrum. The $r = 3"$ case is already presented in the main text (Fig. 5). For Cicone et al. (2015), we report their best–fit parameters and fluxes for the "narrow" $(-200, 200)\,\rm km\,s^{-1}$ component defined in their study. We find good agreement for all apertures between this work and previous studies. This demonstrates that most of the excess flux in larger apertures ($r \gtrsim 3"$) described in Cicone et al. (2015) is due to the reported presence of blue/red–shifted components with large spatial offsets which are not recovered in this work, as discussed in Section 4.

E. CONTINUUM SUBTRACTION AND MASKING OF THE [C II]$_{158\,\mu\rm m}$ LINE

In this appendix, we provide details on the continuum subtraction procedures, focussing on the [C II]$_{158\,\mu\rm m}$ spectral setup. Figure 16 shows the aperture-integrated [C II]$_{158\,\mu\rm m}$ spectrum for various half-width masking regions ranging from $4.5 \times \rm FWHM([CII]) = 1733\,km\,s^{-1}$ to $0.5 \times \rm FWHM([CII]) = 193\,km\,s^{-1}$. In all cases we fit a single and double Gaussian models to the [C II]$_{158\,\mu\rm m}$ emission (as in Section 4.1) and find no evidence to reject the single Gaussian model in favor of a double Gaussian emission profile. Finally, Figure 17 shows the dust continuum measurement as a function of the masking half-width. The continuum is predictably higher for small masking regions, but has converged at the masking half-width adopted in this paper ($1.25 \times \rm FWHM([CII])$).

F. CHANNEL AND MOMENTS MAPS OF THE [C II]$_{158\,\mu\rm m}$ EMISSION

In this appendix, we present additional visualizations of the [C II]$_{158\,\mu\rm m}$ emission velocity structure in J1148+5251. Firstly, we present channel maps in Figure 18 with a channel width of $117\,\rm km\,s^{-1}$. No significant emission ($> 3\sigma$) is

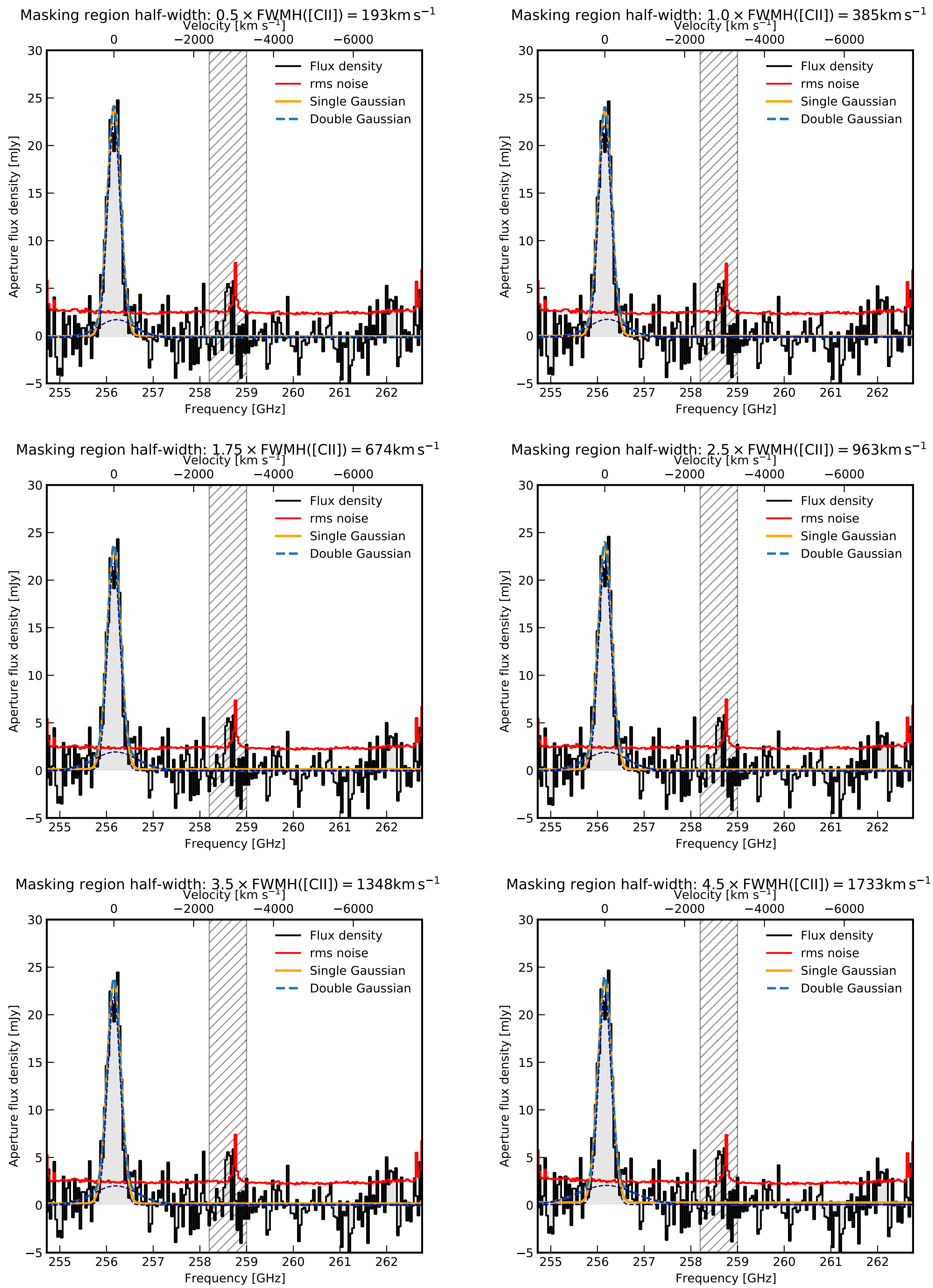

Figure 16. Spectra of the [C II]$_{158\,\mu\mathrm{m}}$ line for different continuum subtractions. The line half-width masking region is indicated in the title of each panel. The colors and symbols are the same as in Figure 5.

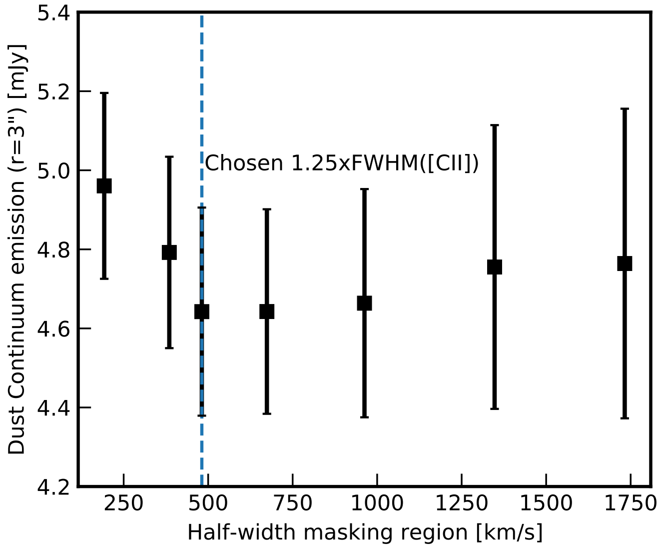

Figure 17. Aperture-integrated continuum flux density at 259 GHz as a function of the line masking half-width. The measurement has converged at the adopted masking width of $1.25 \times \mathrm{FWHM}([\mathrm{CII}])$.

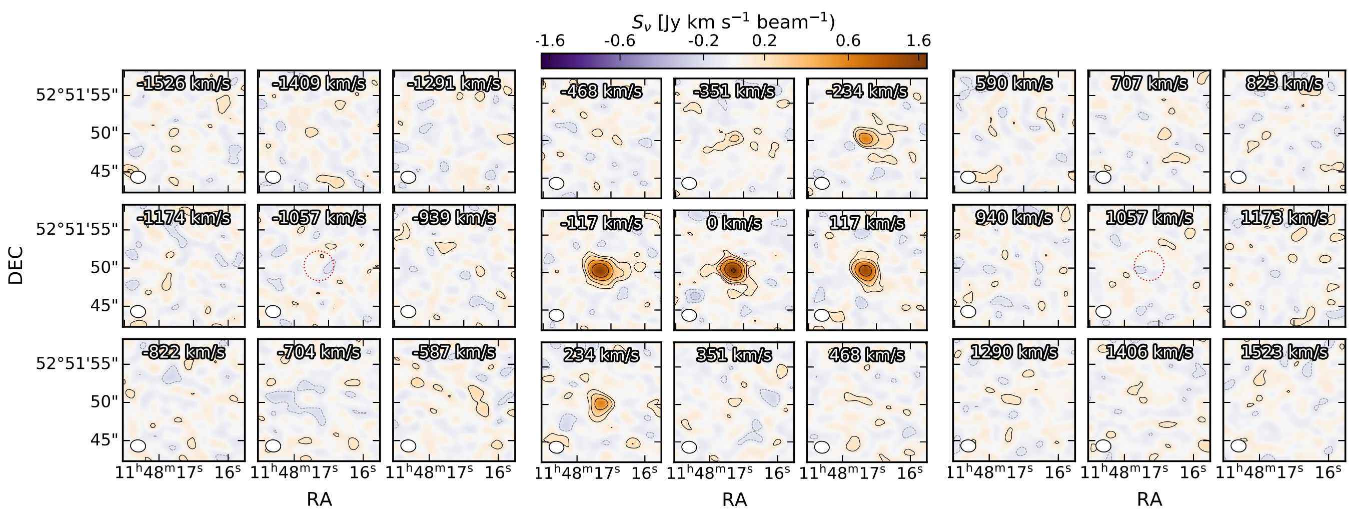

Figure 18. Channel map of the [C II]$_{158\,\mu\mathrm{m}}$ line of J1148+5251, in channels of $117\,\mathrm{km\,s^{-1}}$. The contours are logarithmic $(-8, -4, -2, 2, 4, 8, 16, 32)\sigma$ (rms). The colour scaling is log–linear, the threshold being at 3σ (rms). The colour scaling is log–linear, the threshold being at 3σ (rms).

detected at large radii or at velocity offsets $> 400\,\mathrm{km\,s^{-1}}$ from the peak of the [C II]$_{158\,\mu\mathrm{m}}$ line (cf. Cicone et al. 2015). Secondly, we present the integrated flux, mean velocity and velocity dispersion (so–called moment maps) in Figure 19. These maps are generated using *Qubefit* (Neeleman et al. 2020) using all [C II]$_{158\,\mu\mathrm{m}}$ voxels detected at SN> 3 and standard parameters. We find no kinematic evidence for a bulge–dominated dispersion or a rotating disk model.

REFERENCES

Bañados, E., Decarli, R., Walter, F., et al. 2015, The Astrophysical Journal, 805, L8, doi: 10.1088/2041-8205/805/1/L8

Bañados, E., Venemans, B. P., Mazzucchelli, C., et al. 2018, Nature, 553, 473, doi: 10.1038/nature25180

Beelen, A., Cox, P., Benford, D. J., et al. 2006, The Astrophysical Journal, 642, 694, doi: 10.1086/500636

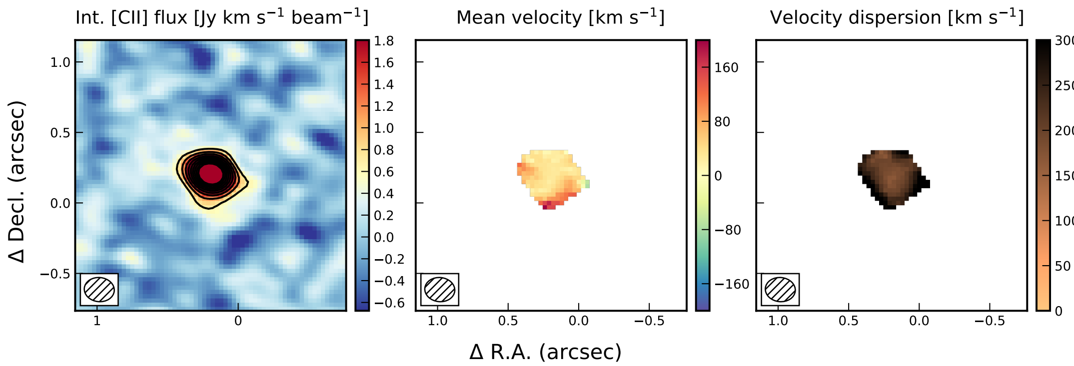

Figure 19. Moment maps of the [C II]$_{158\,\mu m}$ emission. The integrated velocity and velocity dispersion are only shown in pixels at the 3σ level. The absence of any velocity structure is expected given the 3σ detected area covers only ~ 4 beams.

Bertoldi, F., Carilli, C. L., Cox, P., et al. 2003a, Astronomy & Astrophysics, 406, L55, doi: 10.1051/0004-6361:20030710

Bertoldi, F., Cox, P., Neri, R., et al. 2003b, Astronomy & Astrophysics, 409, L47, doi: 10.1051/0004-6361:20031345

Bischetti, M., Maiolino, R., Carniani, S., et al. 2019, Astronomy & Astrophysics, 630, A59, doi: 10.1051/0004-6361/201833557

Bosman, S. E. I. 2020, ZENODO, 10.5281/ZENODO.3634965, doi: 10.5281/ZENODO.3634965

Brauher, J. R., Dale, D. A., & Helou, G. 2008, The Astrophysical Journal Supplement Series, 178, 280, doi: 10.1086/590249

Carilli, C., & Walter, F. 2013, Annual Review of Astronomy and Astrophysics, 51, 105, doi: 10.1146/annurev-astro-082812-140953

Cicone, C., Maiolino, R., Gallerani, S., et al. 2015, Astronomy and Astrophysics, 574, 14, doi: 10.1051/0004-6361/201424980

Costa, T., Sijacki, D., & Haehnelt, M. G. 2014, Monthly Notices of the Royal Astronomical Society, 444, 2355, doi: 10.1093/mnras/stu1632

Croxall, K. V., Smith, J. D., Pellegrini, E., et al. 2017, The origins of [C II] emission in local star-forming galaxies, arXiv, doi: 10.3847/1538-4357/aa8035

Da Cunha, E., Groves, B., Walter, F., et al. 2013, Astrophysical Journal, 766, 13, doi: 10.1088/0004-637X/766/1/13

De Breuck, C., Weiß, A., Béthermin, M., et al. 2019, Astronomy and Astrophysics, 631, A167, doi: 10.1051/0004-6361/201936169

De Looze, I., Cormier, D., Lebouteiller, V., et al. 2014, Astronomy & Astrophysics, 568, A62, doi: 10.1051/0004-6361/201322489

De Rosa, G., Venemans, B. P., Decarli, R., et al. 2014, Astrophysical Journal, 790, 145, doi: 10.1088/0004-637X/790/2/145

Decarli, R., Walter, F., Carilli, C., et al. 2014, Astrophysical Journal, 782, 78, doi: 10.1088/0004-637X/782/2/78

Decarli, R., Walter, F., Venemans, B. P., et al. 2018, The Astrophysical Journal, 854, 97, doi: 10.3847/1538-4357/aaa5aa

Decarli, R., Dotti, M., Bañados, E., et al. 2019a, The Astrophysical Journal, 880, 157, doi: 10.3847/1538-4357/ab297f

Decarli, R., Mignoli, M., Gilli, R., et al. 2019b, Astronomy & Astrophysics, 631, L10, doi: 10.1051/0004-6361/201936813

Di Matteo, T., Springel, V., & Ilernquist, L. 2005, Nature, 433, 604, doi: 10.1038/nature03335

Díaz-Santos, T., Armus, L., Charmandaris, V., et al. 2017, The Astrophysical Journal, 846, 32, doi: 10.3847/1538-4357/aa81d7

Dunne, L., Eales, S. A., & Edmunds, M. G. 2003, A census of metals at high and low redshift and the connection between submillimetre sources and spheroid formation, Oxford Academic, doi: 10.1046/j.1365-8711.2003.06440.x

Fan, X., Strauss, M. A., Schneider, D. P., et al. 2003, The Astronomical Journal, 125, 1649, doi: 10.1086/368246

Ferkinhoff, C., Hailey-Dunsheath, S., Nikola, T., et al. 2010, Astrophysical Journal Letters, 714, 147, doi: 10.1088/2041-8205/714/1/L147

Ferkinhoff, C., Brisbin, D., Nikola, T., et al. 2011, Astrophysical Journal Letters, 740, 29, doi: 10.1088/2041-8205/740/1/L29

Ferland, G. J., Chatzikos, M., Guzmán, F., et al. 2017, The 2017 release of Cloudy, Universidad Nacional Autonoma de Mexico, doi: 10.5281/zenodo.4110791

Foreman-Mackey, D., Hogg, D. W., Lang, D., & Goodman, J. 2013, Publications of the Astronomical Society of the Pacific, 125, 306, doi: 10.1086/670067

Gallerani, S., Ferrara, A., Neri, R., & Maiolino, R. 2014, Monthly Notices of the Royal Astronomical Society, 445, 2848, doi: 10.1093/mnras/stu2031

Gullberg, B., De Breuck, C., Vieira, J. D., et al. 2015, Monthly Notices of the Royal Astronomical Society, 449, 2883, doi: 10.1093/mnras/stv372

Harris, C. R., Jarrod Millman, K., van der Walt, S. J., et al. 2020, Nature, 585, 357, doi: 10.1038/s41586-020-2649-2

Hashimoto, T., Inoue, A. K., Tamura, Y., et al. 2019, Publications of the Astronomical Society of Japan, 71, 71, doi: 10.1093/pasj/psz094

Helou, G., Soifer, B. T., & Rowan-Robinson, M. 1985, The Astrophysical Journal, 298, L7, doi: 10.1086/184556

Herrera-Camus, R., Sturm, E., Graciá-Carpio, J., et al. 2018, The Astrophysical Journal, 861, 94, doi: 10.3847/1538-4357/aac0f6

Högbom, J. A. 1974, Aperture Synthesis with a Non-Regular Distribution of Interferometer Baselines, Tech. rep. https://ui.adsabs.harvard.edu/abs/1974A%26AS...15..417H/abstract

Hunter, J. D. 2007, Computing in Science & Engineering, 9, 90, doi: 10.1109/MCSE.2007.55

Ishibashi, W., & Fabian, A. C. 2015, Monthly Notices of the Royal Astronomical Society, 451, 93, doi: 10.1093/mnras/stv944

Izumi, T., Onoue, M., Matsuoka, Y., et al. 2021a. https://arxiv.org/abs/2101.01199

Izumi, T., Matsuoka, Y., Fujimoto, S., et al. 2021b. https://arxiv.org/abs/2104.05738

Jorsater, S., & van Moorsel, G. A. 1995, The Astronomical Journal, 110, 2037, doi: 10.1086/117668

Katz, H., Kimm, T., Haehnelt, M. G., et al. 2019, Monthly Notices of the Royal Astronomical Society, 483, 1029, doi: 10.1093/mnras/sty3154

Katz, H., Kimm, T., Sijacki, D., & Haehnelt, M. G. 2017, Monthly Notices of the Royal Astronomical Society, 468, 4831, doi: 10.1093/mnras/stx608

Kennicutt, R. C. 1998, Annual Review of Astronomy and Astrophysics, 36, 189, doi: 10.1146/annurev.astro.36.1.189

Kennicutt, R. C., & Evans, N. J. 2012, Star formation in the milky way and nearby galaxies, doi: 10.1146/annurev-astro-081811-125610

King, A. R. 2010, AGN have underweight black holes and reach Eddington, Oxford Academic, doi: 10.1111/j.1745-3933.2010.00938.x

Koudmani, S., Henden, N. A., & Sijacki, D. 2021, Monthly Notices of the Royal Astronomical Society, doi: 10.1093/mnras/stab677

Lagache, G., Cousin, M., & Chatzikos, M. 2018, Astronomy and Astrophysics, 609, 130, doi: 10.1051/0004-6361/201732019

Leipski, C., Meisenheimer, K., Klaas, U., et al. 2010, Astronomy and Astrophysics, 518, L34, doi: 10.1051/0004-6361/201014718

Li, J., Wang, R., Cox, P., et al. 2020, The Astrophysical Journal, 900, 131, doi: 10.3847/1538-4357/ababac

Maiolino, R., Cox, P., Caselli, P., et al. 2005, Astronomy and Astrophysics, 440, 51, doi: 10.1051/0004-6361:200500165

Maiolino, R., Gallerani, S., Neri, R., et al. 2012, Monthly Notices of the Royal Astronomical Society: Letters, 425, L66, doi: 10.1111/j.1745-3933.2012.01303.x

Mazzucchelli, C., Bañados, E., Venemans, B. P., et al. 2017, The Astrophysical Journal, 849, 91, doi: 10.3847/1538-4357/aa9185

Neeleman, M., Prochaska, J. X., Kanekar, N., et al. 2020, ascl, ascl:2005.013. https://ui.adsabs.harvard.edu/abs/2020ascl.soft05013N/abstract

Neeleman, M., Bañados, E., Walter, F., et al. 2019, The Astrophysical Journal, 882, 10, doi: 10.3847/1538-4357/ab2ed3

Neeleman, M., Novak, M., Venemans, B. P., et al. 2021, 12, 2021. https://arxiv.org/abs/2102.05679

Negri, A., & Volonteri, M. 2017, Monthly Notices of the Royal Astronomical Society, 467, 3475, doi: 10.1093/mnras/stx362

Neri, R., Downes, D., Cox, P., & Walter, F. 2014, Astronomy and Astrophysics, 562, 35, doi: 10.1051/0004-6361/201322528

Novak, M., Bañados, E., Decarli, R., et al. 2019, The Astrophysical Journal, 881, 63, doi: 10.3847/1538-4357/ab2beb

Novak, M., Venemans, B. P., Walter, F., et al. 2020, The Astrophysical Journal, 904, 131, doi: 10.3847/1538-4357/abc33f

Oberst, T. E., Parshley, S. C., Stacey, G. J., et al. 2006, The Astrophysical Journal, 652, L125, doi: 10.1086/510289

Oppenheimer, B. D., Davies, J. J., Crain, R. A., et al. 2020, Monthly Notices of the Royal Astronomical Society, 491, 2939, doi: 10.1093/mnras/stz3124

Pavesi, R., Riechers, D. A., Faisst, A. L., Stacey, G. J., & Capak, P. L. 2019, The Astrophysical Journal, 882, 168, doi: 10.3847/1538-4357/ab3a46

Pavesi, R., Riechers, D. A., Capak, P. L., et al. 2016, The Astrophysical Journal, 832, 151, doi: 10.3847/0004-637x/832/2/151

Pensabene, A., Decarli, R., Bañados, E., et al. 2021. https://arxiv.org/abs/2105.09958

Richardson, M. L. A., Scannapieco, E., Devriendt, J., et al. 2016, The Astrophysical Journal, 825, 83, doi: 10.3847/0004-637x/825/2/83

Riechers, D. A., Walter, F., Bertoldi, F., et al. 2009, Astrophysical Journal, 703, 1338, doi: 10.1088/0004-637X/703/2/1338

Robson, I., Priddey, R. S., Isaak, K. G., & McMahon, R. G. 2004, Monthly Notices of the Royal Astronomical Society, 351, L29, doi: 10.1111/j.1365-2966.2004.07923.x

Savage, B. D., & Sembach, K. R. 1996, Annual Review of Astronomy and Astrophysics, 34, 279, doi: 10.1146/annurev.astro.34.1.279

Shao, Y., Wang, R., Jones, G. C., et al. 2017, The Astrophysical Journal, 845, 138, doi: 10.3847/1538-4357/aa826c

Shao, Y., Wang, R., Carilli, C. L., et al. 2019, The Astrophysical Journal, 876, 99, doi: 10.3847/1538-4357/ab133d

Silk, J., & Rees, M. J. 1998, Astronomy and Astrophysics, 331, L1. https://arxiv.org/abs/9801013

Solomon, P. M., Downes, D., Radford, S. J. E., & Barrett, J. W. 1997, The Astrophysical Journal, 478, 144, doi: 10.1086/303765

Springel, V., Di Matteo, T., & Hernquist, L. 2005, Monthly Notices of the Royal Astronomical Society, 361, 776, doi: 10.1111/j.1365-2966.2005.09238.x

The Astropy Collaboration, A., Price-Whelan, A. M., Sipcz, B. M., et al. 2018, The Astronomical Journal, Volume 156, Issue 3, article id. 123, 19 pp. (2018)., 156, doi: 10.3847/1538-3881/aabc4f

Vallini, L., Gallerani, S., Ferrara, A., Pallottini, A., & Yue, B. 2015, Astrophysical Journal, 813, 36, doi: 10.1088/0004-637X/813/1/36

Venemans, B., Walter, F., Neeleman, M., et al. 2020. https://arxiv.org/abs/2010.14874

Venemans, B. P., Walter, F., Decarli, R., et al. 2017a, The Astrophysical Journal, 851, L8, doi: 10.3847/2041-8213/aa943a

—. 2017b, The Astrophysical Journal, 837, 146, doi: 10.3847/1538-4357/aa62ac

Venemans, B. P., Decarli, R., Walter, F., et al. 2018, The Astrophysical Journal, 866, 159, doi: 10.3847/1538-4357/aadf35

Virtanen, P., Gommers, R., Oliphant, T. E., et al. 2020, Nature Methods, 17, 261, doi: 10.1038/s41592-019-0686-2

Wakker, B. P., & Schwarz, U. J. 1988, The Multi-Resolution CLEAN and its application to the short-spacing problem in interferometry, Tech. Rep. 1-2. https://ui.adsabs.harvard.edu/abs/1988A%26A...200..312W/abstract

Walter, F., & Brinks, E. 1999, The Astronomical Journal, 118, 273, doi: 10.1086/300906

Walter, F., Brinks, E., de Blok, W. J. G., et al. 2008, Astronomical Journal, 136, 2563, doi: 10.1088/0004-6256/136/6/2563

Walter, F., Carilli, C., Bertoldi, F., et al. 2004, The Astrophysical Journal, 615, L17, doi: 10.1086/426017

Walter, F., Riechers, D., Cox, P., et al. 2009a, Nature, 457, 699, doi: 10.1038/nature07681

Walter, F., Wei, A., Riechers, D. A., et al. 2009b, Astrophysical Journal, 691, doi: 10.1088/0004-637X/691/1/L1

Walter, F., Bertoidl, F., Carilli, C., et al. 2003, Nature, 424, 406, doi: 10.1038/nature01821

Walter, F., Riechers, D., Novak, M., et al. 2018, The Astrophysical Journal, 869, L22, doi: 10.3847/2041-8213/aaf4fa

Wang, F., Yang, J., Fan, X., et al. 2021. https://arxiv.org/abs/2101.03179

Wang, R., Wagg, J., Carilli, C. L., et al. 2013, Astrophysical Journal, 773, 44, doi: 10.1088/0004-637X/773/1/44

Wang, R., Shao, Y., Carilli, C. L., et al. 2019. https://arxiv.org/abs/1904.07749

Weiß, A., Downes, D., Henkel, C., & Walter, F. 2005, Astronomy & Astrophysics, 429, L25, doi: 10.1051/0004-6361:200400085

Weiß, A., Henkel, C., Downes, D., & Walter, F. 2003, Astronomy & Astrophysics, 409, L41, doi: 10.1051/0004-6361:20031337

Willott, C. J., McLure, R. J., & Jarvis, M. J. 2003, The Astrophysical Journal, 587, L15, doi: 10.1086/375126

Yang, J., Wang, F., Fan, X., et al. 2020, The Astrophysical Journal, 897, L14, doi: 10.3847/2041-8213/ab9c26

Zhao, Y., Lu, N., Xu, C. K., et al. 2016, The Astrophysical Journal, 819, 69, doi: 10.3847/0004-637X/819/1/69